Petroleum Science 23 (2026) 84–102

Contents lists available at ScienceDirect

Petroleum Science

journal homepage: www.keaipublishing.com/en/journals/petroleum-science

Original Paper

Differential hydrocarbon enrichment in Ordovician strata controlled by intra-cratonic ultra-deep strike-slip fault movements, eastern Shunbei area, Tarim Basin, China: Constraints from in-situ calcite U-Pb dating and fluid inclusions

Zhuo Liu [a,b], Jin-Qiang Tian [a,b,*], Fang Hao [a,b,**], Yong-Li Liu [c], Meng-Ting Hang [a,b], Fei-Fei Yuan [d], Fu-Yun Cong [a,b]

[a] State Key Laboratory of Deep Oil and Gas, China University of Petroleum (East China), Qingdao, 266580, Shandong, China
[b] School of Geosciences, China University of Petroleum (East China), Qingdao, 266580, Shandong, China
[c] Research Institute of Exploration and Development, Northwest Oilfield Company, SINOPEC, Urumqi, 830011, Xinjiang, China
[d] School of Geosciences, Yangtze University, Wuhan, 430100, Hubei, China

ARTICLE INFO

Article history:
Received 7 March 2025
Received in revised form
30 June 2025
Accepted 11 September 2025
Available online 17 September 2025

Edited by Xi Zhang and Jie Hao

Keywords:
Strike-slip faults
Calcite U-Pb dating
Fluid inclusion
Ordovician reservoir
Tarim Basin

ABSTRACT

Intracratonic strike-slip faults in central-western China's Tarim Basin serve as critical conduits for hydrocarbon migration and accumulation. This study integrates geochemical characterization, in-situ calcite U-Pb geochronology, and fluid inclusion microthermometry to resolve the long-debated temporal relationships between tectonic reactivation and hydrocarbon charging processes in the ultra-deep Shunbei fault system. Through systematic analysis of reservoir oils and fracture-filling calcites from the Shunbei Nos. 4, 6, and 8 fault zones, we establish a novel chronological framework combining differential hydrocarbon accumulation with fault activation phases. Building upon previous structural analyses, our U-Pb geochronology resolves four distinct tectonic phases for the No. 4 fault: Middle–Late Caledonian (473 ± 12 Ma and 443 ± 17 Ma), Late Caledonian–Early Hercynian, Middle–Late Hercynian, and Indosinian–Yanshanian, while the No. 8 fault exhibits four episodes spanning Middle–Late Caledonian (453.5 ± 2.5 Ma, 413 ± 29 Ma) to Indosinian-Yanshanian (196 ± 57 Ma). Hydrocarbon charging occurred through four discrete phases, with No. 8 fault demonstrating earlier petroleum emplacement (principal oil: 294 ± 29 Ma; principal gas: 196 ± 57 Ma) relative to No. 4 fault (principal oil: 282–205 Ma; principal gas: 196–11 Ma). MDR-MPI-1 correlations reveal hydrothermal influence on select oils, causing maturity overestimation. Fluorescence spectra (λ_{max} <445 nm) and geochemical indices (vitrinite reflectance equivalent: 1.2%–1.6%) confirm high thermal maturity. Stable carbon isotopes ($\delta^{13}C_1 < \delta^{13}C_2$) confirm normal genetic oil-type gas with low thermal maturity. Diamondoid indices and gas compositional trends ($\ln(C_2/C_3)$ vs. $\delta^{13}C_2$–$\delta^{13}C_3$) demonstrate predominant kerogen-derived methane with subordinate oil-cracked contributions. Enhanced vertical connectivity and elevated source maturity in No. 8 fault account for its preferential hydrocarbon enrichment. This work establishes a genetic linkage between multi-phase fault activation and differential hydrocarbon accumulation, providing an innovative methodology for evaluating ultra-deep reservoirs in cratonic basins through coupled geochronological-hydrocarbon fluid inclusion analysis.

* Corresponding author.
** Corresponding author.
E-mail addresses: tianjq@upc.edu.cn (J.-Q. Tian), haofang@cug.edu.cn (F. Hao).
Peer review under the responsibility of China University of Petroleum (Beijing).

https://doi.org/10.1016/j.petsci.2025.09.022

1. Introduction

In the Tarim Basin of Northwestern China, intra-cratonic strike-slip faults serve as critical hydrocarbon-bearing structures within superimposed basins (Cong et al., 2024a; Jia et al., 2022; Ma et al., 2022; Qi et al., 2024). These faults develop through the reactivation of pre-existing intraplate structures under localized stress concentration (Aydin and Berryman, 2010; Chen, 2023; Mann, 2007). Characterized by slip displacements on the order of hundreds of meters, weak activity, and steep dip angles, these features are often challenging to identify (Aydin and Berryman, 2010; Deng et al., 2019; Mann, 2007). Traditional methods for analyzing fault activity stages predominantly rely on seismic data interpretation (Qiu et al., 2019; Teng et al., 2020; Wang et al., 2022b); however, such approaches frequently encounter limitations in precisely constraining the timing of fault movements (Wu et al., 2021). Superimposed basins exhibit structural complexity due to multiple phases of tectonic activity, which often obscure evidence of early faulting (He et al., 2023; Tang et al., 2023; Wang et al., 2022b; Wu et al., 2021). A prominent example is the Shunbei Oil and Gas Field, located in the Taklamakan Desert of the Tarim Basin, which represents China's archetypal ultra-deep, fault-controlled hydrocarbon system (Cao et al., 2020; Deng et al., 2022; Ma et al., 2022; Yun, 2021a, 2021b). Challenges in resolving fault activity timing here are compounded by (1) inherent difficulties in identifying intra-cratonic strike-slip faults in ultra-deep (>7500 m) desert strata with reduced seismic resolution, (2) limitations of conventional seismic methods, and (3) structural overprinting in superimposed basins (Chen, 2023; Jia et al., 2022; Wu et al., 2021; Yang et al., 2022a).

The spatial distribution of Shunbei hydrocarbon reservoirs is structurally controlled by strike-slip faults, with reservoir widths (300–1600 m) reflecting fault activity intensity and architecture (Yun et al., 2025). Regionally, oil predominates in western fault zones, while gas enriches eastern domains, with both concentrated along major faults (Yun, 2021b). Crude oils are predominantly medium-to light-grade (Yun, 2021a). Previous studies of hydrocarbon enrichment in the Shunbei West Area (No. 1 and No. 5 faults) have employed oil geochemistry and fluid inclusion analyses to identify two to three distinct charging phases, predominantly during the Late Hercynian to Himalayan periods (Cong et al., 2024a, 2024b; Liu et al., 2023; Ma et al., 2022; Qi, 2020; Wang et al., 2021; 2024; Zhang et al., 2023a). West-to-east samples (No.7→No.5→No.1) exhibit increasing Pr/n-C_{17}, and Ph/n-C_{18} ratios with thermal maturity, while Pr/Ph, ACA, and S1-class alkylation decrease, accompanied by DBT/P and MDR increases, and confirmed methylphenanthrene/methylbiphenyl/MDBT isomer conversion pathways (Xu et al., 2022, 2024). Previous studies utilizing calcite vein U-Pb dating have revealed that the Shunbei No. 1, No. 5, and No. 7 strike-slip faults underwent multiple reactivations during the Mid-Caledonian to Mid-Hercynian (449 ± 10 to 326 ± 15 Ma), Mid-Caledonian to Indosinian (471 ± 12 Ma to 241 ± 15 Ma), and Mid-to Late-Caledonian (466.7 ± 2.8 to 444 ± 12 Ma) periods, respectively (Dong et al., 2025; Cong et al., 2024b; Li et al., 2023).

In contrast, the Shunbei East Area (No. 4, No. 6, and No. 8 faults) exhibits substantial resource potential, with hydrocarbon abundances reaching 132×10^4 t/km^2, 27.5×10^8 m^3/km^2, and 17.4×10^8 m^3/km^2, respectively (Qi et al., 2021). Geochemical investigations of these eastern faults—utilizing molecular biomarkers, carbon isotopes, aromatic hydrocarbons, light hydrocarbons, and diamondoid compositions—reveal distinct fluid characteristics (Bian et al., 2023; Ma and Qi, 2023; Peng et al., 2024; Qiao et al., 2024a; Zhang et al., 2024). Crude oil maturity in the No. 4 fault ranges from 1.14% to 1.60% (equivalent to vitrinite reflectance, R_o), while associated natural gas exhibits maturities of 1.30%–1.70% R_o (Ma and Qi, 2023; Peng et al., 2024; Zhang et al., 2024). Although localized thermal sulfate reduction (TSR) effects are observed in Ordovician reservoirs, these processes show no significant impact on current crude oil compositions (Qiao et al., 2024a). Calcite vein U-Pb geochronology has revealed that the Shunbei No. 4 strike-slip fault experienced multiple reactivation episodes spanning the Mid-Caledonian (449 ± 15 Ma) to Indosinian (307.9 ± 82.1 Ma) periods, reflecting prolonged tectonic activity (Li et al., 2023; Peng et al., 2024; Song et al., 2022). For the No. 6 fault, integrated stratigraphic and structural analyses have delineated a three-stage evolutionary model: Early Caledonian initiation, Mid-Caledonian maturation, and Late Caledonian to Hercynian reactivation, as evidenced by fault stratigraphy variations and planar distribution patterns (Liu et al., 2025; Zhang et al., 2023b). Geophysical investigations of the No. 8 fault further propose a four-phase tectonic history: Mid-Caledonian oblique compression, Late Caledonian–Early Hercynian transtension, Mid-Late Hercynian reactivation, and Indosinian to Yanshanian structural overprinting (Yun, 2021a). Despite these advances, key uncertainties persist regarding hydrocarbon enrichment mechanisms in the Shunbei East Area, attributed to three factors: (1) delayed exploration (initiated in 2019 by Sinopec Northwest Oilfield Company) relative to western counterparts (Cao et al., 2024); (2) extreme reservoir depths (7500–8051 m in the $O_{1-2}y$ (Lower–Middle Ordovician Yingshan Formation) and O_2yj (Middle Ordovician Yijianfang Formation), limiting core availability and necessitating reliance on fluid-based geochemical proxies (Cao et al., 2024; Ma et al., 2022); and (3) complex ultra-deep hydrocarbon migration histories that challenge conventional geochemical interpretations (Peng et al., 2024).

While traditional seismic methods have advanced fault characterization in sedimentary basins, their limited temporal resolution hinders precise correlation between fault activation phases and hydrocarbon migration events—a critical uncertainty addressed in this study through high-precision in situ U-Pb dating of fracture-filling calcite veins. Fracture-filling calcite veins, ubiquitous in sedimentary basins, provide critical records of fluid-rock interactions during tectonic events (Chen et al., 2022; Craddock et al., 2021; Lueck et al., 2021; Yang et al., 2021a; Zhao and Shi, 2019). Recent advances in in situ micro-scale U-Pb dating of calcite enable precise determination of brittle structure activation timing (Roberts and Walker, 2016; Walter et al., 2018; Wu et al., 2021; Yang et al., 2022a; Cong et al., 2022). When combined with fluid inclusion analysis—a robust proxy for hydrocarbon charge history (Cong et al., 2022; Liu Z. et al., 2024; Ping et al., 2020; Wang M. et al., 2020)—these techniques allow direct correlation between fault activity and petroleum migration events (Holdsworth et al., 2019; Rochelle-Bates et al., 2021; Cong et al., 2023). Integration of U-Pb chronometry with petroleum maturity data, quantitative fluorescence spectroscopy, and inclusion-derived charge timing permits identification of “critical moments” in hydrocarbon accumulation (Cong et al., 2024a, 2024b).

This study employs an integrated approach combining petroleum geochemistry, quantitative fluorescence spectroscopy, and in situ calcite U-Pb dating to investigate hydrocarbon enrichment processes in the Shunbei East Area. Specific objectives include: 1. Determining the absolute timing of strike-slip fault activity through U-Pb dating of calcite veins and reconstructing tectonic histories; 2. Establishing chronologies of multi-phase hydrocarbon charging through fluid inclusion analysis within the U-Pb geochronological framework; 3. Identifying principal accumulation events through combined geochemical and temporal

analyses. By elucidating spatiotemporal relationships between fault activation and hydrocarbon migration, we aim to (1) quantify reservoir-forming factors during critical periods, (2) reconstruct differential accumulation processes across distinct strike-slip systems, and (3) advance mechanistic understanding of hydrocarbon enrichment in ultra-deep, fault-controlled settings.

2. Geological setting

Located in Northwestern China, the Tarim Basin represents the country's largest inland sedimentary basin. Bordered by the Tianshan orogenic belt to the north and northwest, the Kunlun orogenic belt to the southwest, and the Altyn orogenic belt to the southeast, this basin constitutes a critical component of Central Asian tectonics (Cong et al., 2021, 2024b; Li et al., 1996; Yao et al., 2018, Fig. 1). Its geological architecture comprises a Paleozoic cratonic basin overprinted by Meso-Cenozoic foreland basins, forming a complex superimposed basin system (Zhang et al., 2015). The Proterozoic basement is overlain by strata ranging from Neoproterozoic to Cambrian in age (Zhang et al., 2013).

The Tarim Basin has undergone a complex multiphase tectonic evolution, which includes the Caledonian orogeny (542–416 Ma, from the Cambrian to the Silurian periods), the Hercynian orogeny (416–251 Ma, from the Devonian to the Permian periods), the Indosinian orogeny (251–199.6 Ma, spanning the Triassic period), the Yanshanian orogeny (199.6–65.5 Ma, from the Jurassic to the Cretaceous periods), and the ongoing Himalayan orogeny (65.5 Ma to the present, spanning the Cenozoic era) (Zhang et al., 2011; Li et al., 2013; Zhu et al., 2019). The Tarim Basin, originating from the Neoproterozoic breakup of the Rodinia supercontinent, evolved from an extensional tectonic regime to a compressional one by the early Ordovician, and has since undergone multiple phases of intense tectonic deformation (Zhang et al., 2013; He et al., 2016).

Structurally, the basin is divided into seven major tectonic units: three uplift belts (Tabei North, Central, Southeast) and four depression belts (Kuqa, Northern, Southwest, Southeast) (He et al., 2016; Fig. 1(b)). The Shuntuoguole Low Uplift, situated within the Northern Depression belt, is bounded by the Awati Depression to the northwest and the Manjiar Depression to the northeast (Deng et al., 2019; Wang et al., 2022a; Fig. 1(b)).

The Shuntuoguole Low Uplift exhibits a stratigraphic transition from marine to non-marine facies during the Sinian–Early Permian, followed exclusively by continental deposition from the Late Permian to Quaternary (Jia and Wei, 2002; Li et al., 1996).

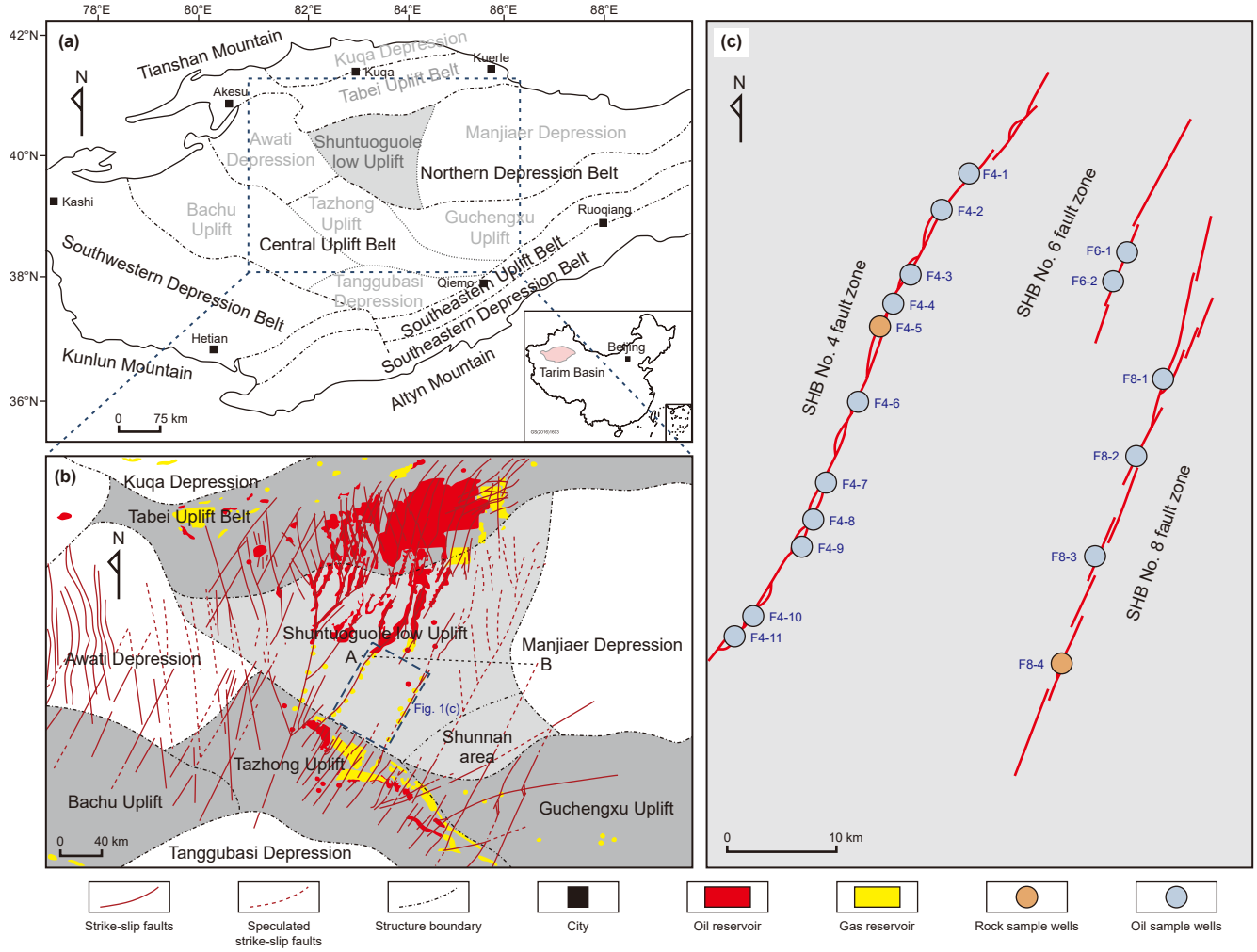

Fig. 1. **(a)** Simplified tectonic framework of the Tarim Basin, Northwestern China (modified from Liu Z. et al., 2024). **(b)** Location of the study area and distribution of major strike-slip faults within the central Tarim Basin (modified from Liu Z. et al., 2024). **(c)** Structural map of the upper surface of the Yijianfang Formation, illustrating the distribution of sampling wells and faults in the Shuntuoguole Low Uplift.

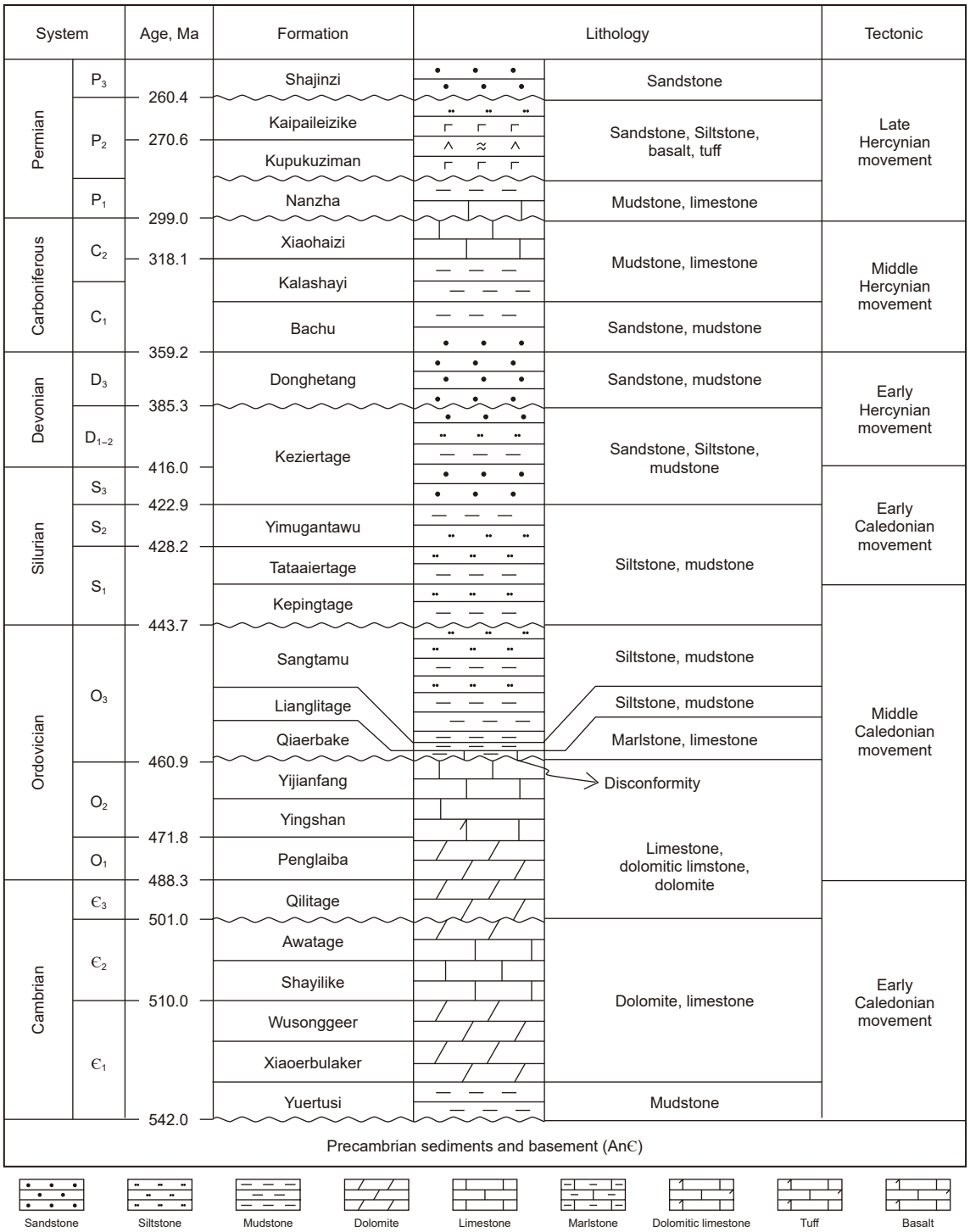

Fig. 2. Generalized stratigraphic column displaying the paleozoic strata and discordances within the Shuntuoguole Low Uplift (modified from Cong et al., 2024a).

Ordovician stratigraphy is subdivided into six formations (Fig. 2): 1. Penglaiba (O_1p) and Lower Yingshan ($O_{1-2}y$): Dolostone-dominated. 2. Upper Yingshan ($O_{1-2}y$) and Yijianfang (O_2yj): Silicified limestone, dolomitic limestone, and limestone—primary reservoir units. 3. Qiaerbake (O_3q), Lianglitage (O_3l), and Sangtamu (O_3s): Argillaceous limestone and mudstone caprocks (Cai and Li, 2008; Lu et al., 2017; Cong et al., 2024b).

The Shunbei area (hereafter referring to the Shuntuoguole Low Uplift) hosts a multi-phase strike-slip fault system with spatially variable orientations and distinct reactivation histories. The No. 5 fault acts as a key structural boundary separating two domains: (1) the Western Domain, dominated by NW-striking faults (Nos. 7, 9, 11; average strike ~20° NW), and (2) the Eastern Domain, characterized by NE-striking faults (Nos. 4, 6, 8; average strike ~30° NE), as documented in Deng et al. (2018) and Ma et al. (2019). Tectonic evolution of the eastern Shunbei fault system involved three sequential phases: initial oblique compression during the Mid-Caledonian III Orogeny, followed by oblique extension and

pure shear deformation in the Late Caledonian–Early Hercynian, and culminating in Mid-Late Hercynian reactivation under basin-margin tectonic stresses, consistent with regional models (Deng et al., 2018; Qiu et al., 2019; Yun, 2021a).

Based on comprehensive analysis and correlation of extensive seismic data, previous studies have revealed a progressive eastward decrease in segmentation quantity accompanied by increased segment length along the Shunbei 4, 6, and 8 strike-slip faults in the eastern Shunbei area, indicating a gradual enhancement of slip displacement (Liu et al., 2023). Seismic profiles demonstrate that the maximum vertical deformation amplitude and lateral shortening magnitude within the translation segments of these strike-slip faults systematically increase from west to east (Deng et al., 2024; Liu et al., 2023). Furthermore, the activity intensity of overlying en-echelon normal faults along the major strike-slip fault zone shows eastward amplification, while the vertical connectivity of underlying principal slip zones exhibits corresponding improvement (Deng et al., 2024; Liu et al., 2023; Yun, 2021a).

3. Samples and methods

3.1. Samples

Core samples containing well-developed fracture-filling calcite veins (see Supplementary Material, Figs S1–S2), along with crude oil and natural gas from the Shunbei No. 4, No. 6, and No. 8 strike-slip fault zones, were selected for integrated geochemical and geochronological analysis. All experiments were conducted at the National Key Laboratory of Deep Oil and Gas, China University of Petroleum (East China).

3.2. Methods

Crude Oil Characterization: Seventeen crude oil samples from the O_2yj and $O_{1-2}y$ formations were analyzed using gas chromatography (GC) and GC-mass spectrometry (GC-MS) to assess maturity. Aromatic and Adamantane Components: Analyzed using an Agilent GC6890-5973MS system with DB-5MS columns (60 m × 0.25 mm × 0.25 μm and 30 m × 0.32 mm × 0.25 μm). Carrier gas flow rates: 1.0 mL/min (aromatics) and 1.8 mL/min (adamantanes). Aromatics: Initial temperature 80 °C (1 min hold), ramped to 310 °C at 3 °C/min (40 min hold). Adamantanes: Initial temperature 50 °C (2 min hold), ramped to 310 °C at 5 °C/min (10 min hold). Light Hydrocarbons: Analyzed using an Agilent GC6890 with a 50 m × 0.20 mm × 0.50 μm HP-PONA column (0.5 mL/min flow). Temperature program: 30 °C (15 min hold) → 70 °C at 1.5 °C/min → 280 °C at 3 °C/min (90 min hold).

Natural gas carbon isotope analysis was carried out on a Thermo Fisher MAT 253plus (GC-IRMS). Carbon Isotope Analysis: Stable carbon isotopes ($\delta^{13}C$) were measured relative to the Vienna Pee Dee Belemnite (VPDB) standard, with a reproducibility of ±0.3‰. Specifically, the carbon isotope analyses of samples were carried out with more than three replicate measurements to enhance precision and reliability, following the calibration protocols outlined by He et al. (2021). Methane, ethane, and propane standards yielded $\delta^{13}C$ values of −43.61‰ ± 0.09‰, −40.24‰ ± 0.10‰, and −33.79‰ ± 0.09‰, respectively (Dai et al., 2012).

Fluid inclusion and mineralogical analysis: Nine core samples from the SHB4 (F4-5 well) and SHB8 (F8-4 well) fault zones were processed into doubly polished thin sections. Samples originated from the Yingshan ($O_{1-2}y$) and Yijianfang (O_2yj) carbonate reservoirs (7700–9000 m depth).

Cathodoluminescence (CL): Performed using a RELIOTRON system to identify carbonate phases and mineral relationships (Celestino et al., 2021). Fluid Inclusion Petrography: Conducted with a NIKON Ni-U microscope (UV light source: 330–380 nm excitation, 420 nm barrier filter). Fluorescence spectra (420–800 nm) were acquired using an Ocean Optics Maya 2000 Pro spectrometer (0.471 nm resolution) and classified by peak wavelength. Raman Spectroscopy: LABHR-VIS LABRAM HR800 spectrometer (532.19 nm laser, 1800 grating, 0.35 cm^{-1} resolution). Methane inclusions were analyzed between 2800 and 3000 cm^{-1}.

Eight calcite veins underwent in situ U-Pb dating using an Applied Spectra RESOlution-LR excimer laser ablation system coupled to an Agilent 7900 ICP-MS. Laser parameters included a 100 μm static spot, 20 Hz frequency, and ~3 J/cm^2 fluence (Wu et al., 2022). Each cycle comprised: 2–3 s pre-ablation, 15 s background acquisition, 20 s ablation, and 25 s washout. Calcite samples and NIST614 standards were analyzed alternately every 10 samples. Data reduction employed LADR_1.1.07 (Norris and Danyushevsky, 2018) for $^{207}Pb/^{206}Pb$ correction, followed by Microsoft® Excel linear correction of $^{238}U/^{206}Pb$ ratios against WC-1 calcite standard, yielding a Tera-Wasserburg age of 254.4 Ma ($^{207}Pb/^{206}Pb = 0.85$). Lower intercept ages were generated using IsoplotR (http://isoplotr.es.ucl.ac.uk/home/index.html) (Vermeesch, 2018) via Tera-Wasserburg concordia regression, with input uncertainties defined as 2σ standard errors (abs), output uncertainties as confidence intervals (abs), and a probability cutoff of 0.05. ASH-15D secondary standard validation produced a $^{238}U/^{206}Pb$ age of 2.909 ± 0.088 Ma (2σ), consistent with published values (Nuriel et al., 2021).

Thermal history modeling: One-dimensional burial/thermal histories for wells F4-5 and F8-4 were modeled using Schlumberger's PetroMod® software. Input parameters included: Stratigraphy, lithology, and depositional ages (SINOPEC well reports). Boundary conditions (erosion events, paleo-water depth, heat flow). Petroleum generation kinetics (Dieckmann et al., 2000). Heat flow evolution based on Li et al. (2010).

4. Results

4.1. Geochemical characteristics of oil and gas

The geochemical characteristics of oils from the Shunbei No. 4, No. 6, and No. 8 strike-slip faults were evaluated using established maturity indices. The methyl dibenzothiophene ratio (MDR = 4-MDBT/1-MDBT; Radke et al., 1986) and methylphenanthrene index (MPI-1 = 1.5 × (3-MP + 2-MP)/(P + 9-MP + 1-MP; Radke, 1988) reveal contrasting maturity trends. While MDR values exhibit a wide range across fault zones (SHB No. 4: 2.74–19.17; SHB No. 8: 4.25–15.10), MPI-1 values remain relatively constrained (1.03–1.40; Fig. 3(a)). Further analysis using methyladamantane (MAI = 1-MA/[1-MA + 2-MA]) and methyldiamantane indices (MDI = 4-MD/[1-MD + 3-MD + 4-MD]; Chen et al., 1996) highlights variations in high thermal maturity. MDI values range from 43.77% to 57.88% in the SHB No. 4 fault and 46.09%–49.79% in the SHB No. 6 and No. 8 faults (Fig. 3(b)). MAI values show limited variability in the SHB No. 4 and No. 6 faults (63.44%–67.75%) but increase significantly in the SHB No. 8 fault (66.51%–73.53%; Fig. 3(b)). Light hydrocarbon analysis (C_5–C_7) yields heptane (H) and isoheptane (I) values of 32.33%–41.62% and 2.74–6.00, respectively (Fig. 3(c)).

Cross-plots of (3- + 4-) methyldibenzothiophene (MD) versus ααα(20R)-C_{29} sterane concentrations (Dahl et al., 1999) further confirm thermal maturity and the extent of oil cracking and destruction, with MD and sterane values spanning 62.4–338.8 ppm and 0.28–3.97 ppm, respectively (Fig. 3(d)). The hydrocarbon generation processes were constrained through genetic characterization of natural gas origins using paired $\delta^{13}C_1$ (−49.48‰ to −44.21‰) and $\delta^{13}C_2$ (−40.31‰ to −36.17‰) values, following the methodologies of Wang et al. (2024) and Zhang et al. (2017)

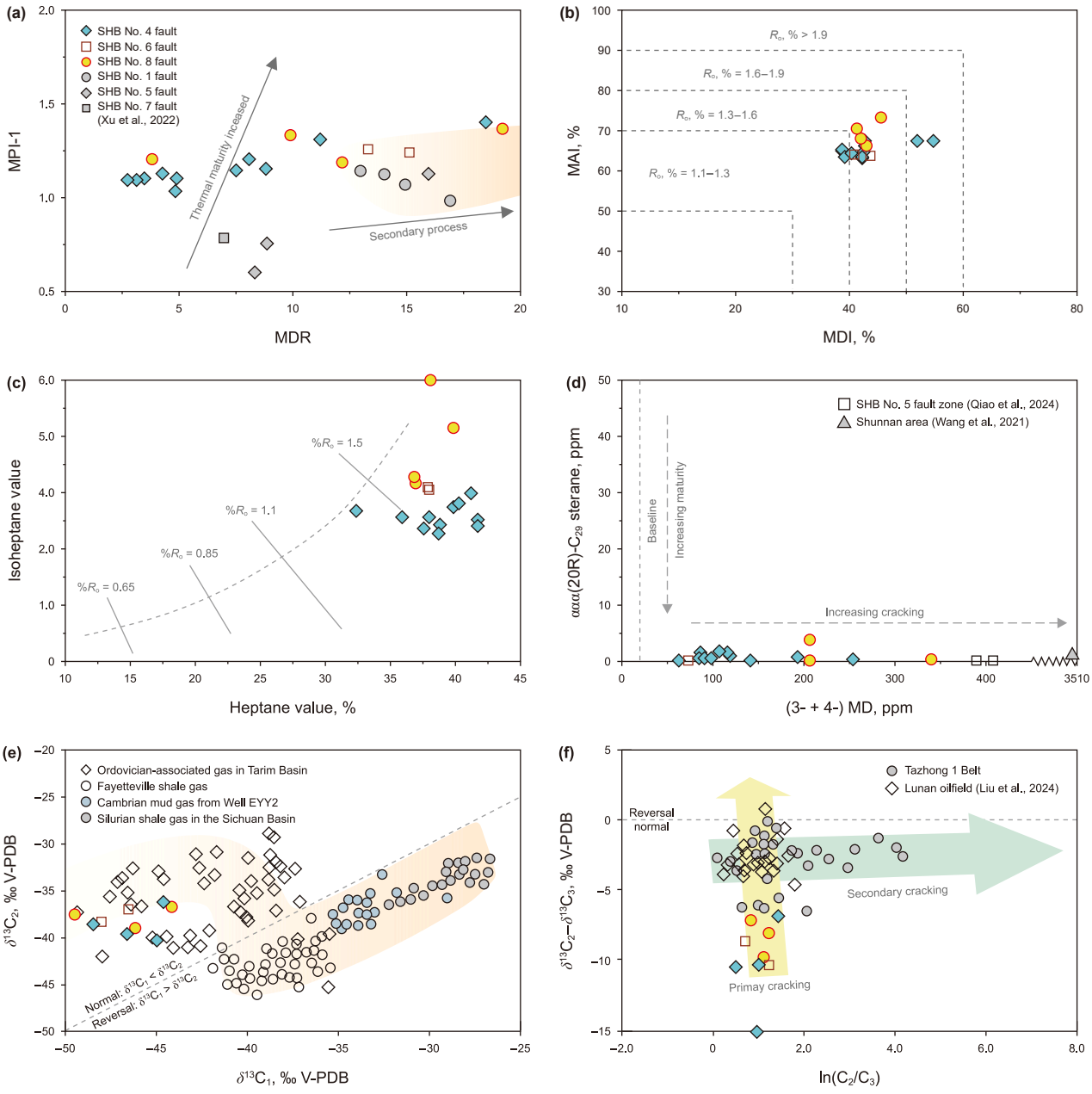

Fig. 3. **(a)** MDR vs. MPI-1 (modified from Xu et al., 2022); **(b)** MDI vs. MAI (after Chen et al., 1996; Zhang et al., 2005); **(c)** Heptane ratio vs. Isoheptane ratio (after Thompson, 1983; Walters et al., 2003); **(d)** Cross-plots of concentrations of (3- + 4-) MD (methyldimantanes) *vs.* ααα20R C_{29} steranes (after Dahl et al., 1999; modified from Wang et al., 2021; Qiao et al., 2024b); **(e)** $\delta^{13}C_1$ *vs.* $\delta^{13}C_2$ (modified from Wang et al., 2024; Zhang et al., 2017, 2021); **(f)** ln(C_2/C_3) *vs.* $\delta^{13}C_2 - \delta^{13}C_3$ (after Prinzhofer and Huc, 1995; modified from Liu X. et al., 2024).

(Fig. 3(e)). Natural gas origin analysis via ln(C_2/C_3) versus ($\delta^{13}C_2$–$\delta^{13}C_3$ (Prinzhofer and Huc, 1995) yields values of 0.48–1.43 and −15.18‰ to −6.86‰, respectively (Fig. 3(f)).

4.2. Calcite vein petrography and u-pb geochronology

In the Shunbei No. 4 fault zone, two distinct calcite vein types fill fractures. The first generation (F4-5-stage I) comprises subhedral to anhedral fine crystals with dark red cathodoluminescence (CL; Fig. 4(b1)–(b2)), yielding a U-Pb age of 473 ± 12 Ma (Fig. 4(b3)). The second generation (F4-5-stage II) consists of euhedral coarse crystals with bright red CL (Fig. 4(c1)–(c2)), dated to 443 ± 17 Ma (Fig. 4(c3)). In Well F8-4 of the same fault zone, four calcite generations are recognized based on CL colors: F8-4-stage I (dark red, 453.5 ± 2.5 Ma; Fig. 5(a3)), F8-4-stage II (orange-yellow, 413 ± 29 Ma; Fig. 5(a4)), F8-4-stage III (dark orange, 294 ± 29 Ma; Fig. 5(b3)), and F8-4-stage IV (bright orange, 196 ± 57 Ma; Fig. 5(b4)).

4.3. Fluid inclusion studies

4.3.1. Hydrocarbons inclusion petrography

Following the classification of Goldstein and Reynolds (1994), hydrocarbon inclusions are categorized as primary or secondary based on their distribution relative to host mineral growth. Primary inclusion assemblages, synchronous with calcite

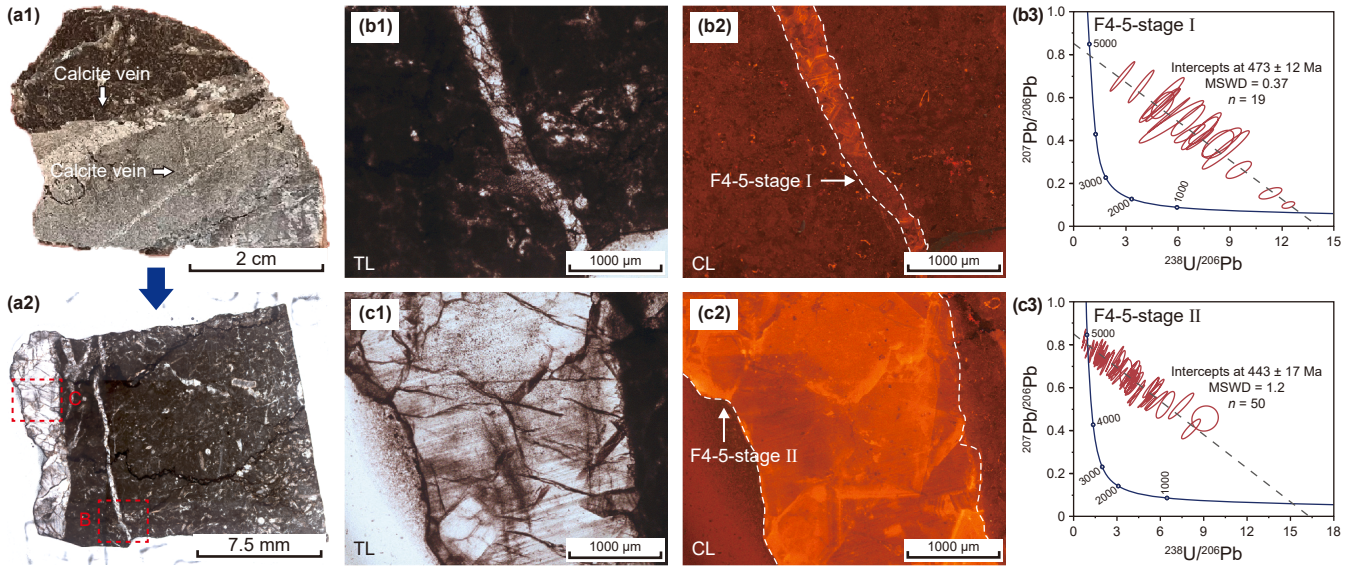

Fig. 4. **(a1)** Hand specimens from well F4-5 in the Yijianfang Formation (7727.28 m) at the SHB No. 4 fault zone, Shuntuoguole Low Uplift. Photomicrographs under transmitted light (TL) **(a2)**, **(b1)** and **(c1)** and cathodoluminescence (CL) microscopy **(b2)** and **(c2)** of sample portions utilized for analysis. Tera-Wasserburg concordia plots displaying $^{238}U/^{206}Pb$ versus $^{207}Pb/^{206}Pb$ ratios from in situ U-Pb dating of calcite veins (F4-5-stage I and F4-5-stage II) from well F4-5 **(b3)** and **(c3)**. Mean squared weighted deviation (MSWD) is also presented.

crystallization, are entrapped along growth bands, cleavage planes, or within cloudy cores of individual crystals (Fig. 6(a2), 6(a3), 7(a2), 7(a3), 7(c2), 7(c3), 7(d2)). Secondary inclusions, postdating calcite formation, occur in linear arrays within healed microfractures that crosscut calcite crystals (Fig. 6(b2), 6(b3), 6(c2), 6(c3), 6(d2), 7(c1), 7(c2)). Fluorescence spectral analysis, quantified by the wavelength of maximum intensity (λ_{max}), was employed to differentiate oil inclusion populations (Cong et al., 2022, 2024b; Liu Z. et al., 2024).

In the F4-5-stage II veins (Fig. 6(a1), 6(b1), 6(c1)), three oil inclusion types were identified, comprising one primary type (yellow-green, λ_{max} = 504.14 nm; Fig. 6(a2)–(a3)) and two secondary types: pale blue (λ_{max} = 472.78 nm; Fig. 6(b2)–(b3)) and dark blue (λ_{max} = 443.54 nm; Fig. 6(c2)–(c3)). Laser Raman spectroscopy of coexisting vapor inclusions confirmed methane as the sole gaseous component (Fig. 6(d1)–(d3)). Primary yellow-green oil inclusions (λ_{max} = 495.07 nm) were observed in F8-4-stage I calcite (Fig. 7(a1)–(a3)), while secondary pale blue inclusions (λ_{max} = 472.32 nm) occur in microfractures (Fig. 7(b1)–(b3)). F8-4-stage III calcite hosts dark blue primary inclusions (λ_{max} = 441.71 nm) along growth bands (Fig. 7(c1)–(c3)), and F8-4-stage IV contains methane-dominated inclusions localized within crystal growth zones (Fig. 7(d1)–(d3)).

4.3.2. Fluorescence spectroscopy

The fluorescence spectral characteristics of the analyzed oil inclusions exhibit systematic variations, as illustrated in Fig. 8. In our study, we collected a total of 296 fluorescence spectroscopic data points, which include 280 quantitative fluorescence spectral data points from oil inclusions and 16 quantitative fluorescence spectral data points from reservoir oils. These data were systematically organized for the No. 4 and No. 8 strike-slip fault zones, as depicted in Fig. 8. The measured λ_{max} values of the oil inclusions and reservoir oils predominantly range from 520 to 415 nm. Three distinct populations of λ_{max} values can be identified within this range: 520–490 nm, 490–450 nm and 450–415 nm. These populations were discerned based on the pronounced peak patterns observed in the histograms of fluorescence wavelengths, as shown in Fig. 8. Notably, the fluorescence wavelength values of the reservoir oils are confined to the third group, with λ_{max} values ranging from 450 to 415 nm. This finding indicates that the crude oils in the reservoirs of the No. 4 and No. 8 strike-slip fault zones are primarily the result of an oil charging event represented by the third group of oil inclusions, which have fluorescence wavelengths ranging from 450 to 415 nm.

4.3.3. Microthermometry

Aqueous inclusion assemblages, which are found coexisting with oil and methane inclusions within fracture-filling calcite veins, have been analyzed (Figs. 9 and 10). The findings indicate that the homogenization temperatures (Th) of aqueous inclusions associated with hydrocarbon inclusions typically span a range from 81 to 156 °C (Figs. 9 and 10).

In well F4-5, Th values of aqueous inclusions coexisting with yellow-green fluorescence oil inclusion assemblages, pale blue fluorescence oil inclusion assemblages, and dark blue fluorescence oil inclusion assemblages are respectively confined to the ranges of 81–92 °C, 96–108 °C, and 116–130 °C (Fig. 9). The homogenization temperature of the aqueous inclusions associated with methane inclusions ranges from 136 to 152 °C (Fig. 9). For well F8-4, Th values associated with pale blue fluorescence oil inclusion assemblages, dark blue fluorescence oil inclusion assemblages, and methane inclusion assemblages are found within the ranges of 84–106 °C, 124–135 °C, and 148–156 °C (Fig. 10).

5. Discussion

5.1. Absolute time frame of strike-slip fault activity in the shunbei No. 4 and No. 8 fault zones

Previous studies of the Shunbei No. 4 strike-slip fault have proposed divergent classifications for its activity history, primarily inferred from seismic data. Interpretations suggest either three phases (Middle Caledonian, Late Caledonian–Early Hercynian, and Middle–Late Hercynian; Liu and Deng, 2022; Liu et al., 2023) or four phases (including an additional Indosinian–Himalayan phase;

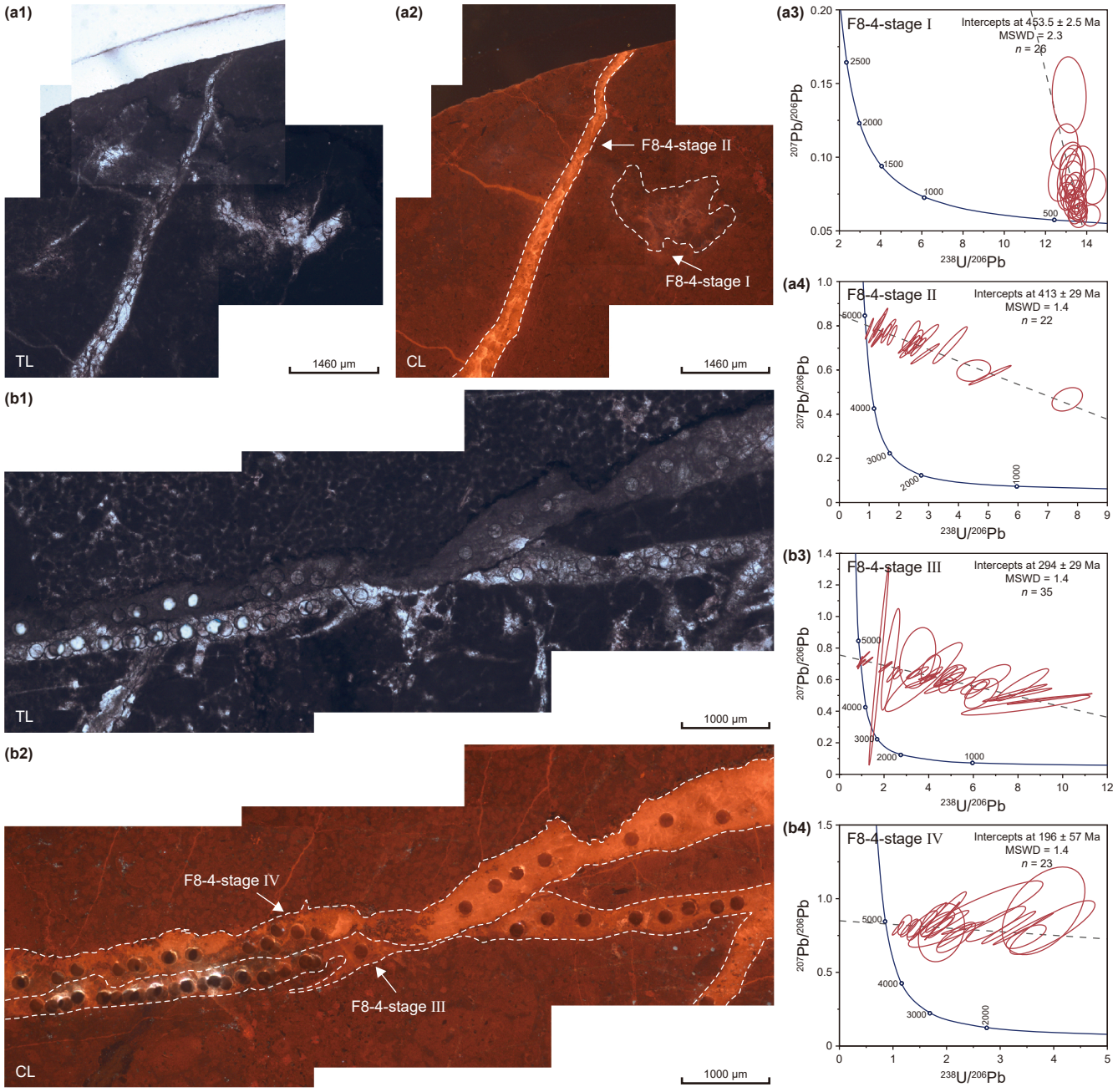

Fig. 5. Four fracture-filling calcite veins/cements from well F8-4 in the Yingshan Formation: F8-4-stage I, F8-4-stage II, F8-4-stage III and F8-4-stage IV **(a1)**, **(a2)**, **(b1)** and **(b2)**. Stage I calcite vein/cement (F8-4-stage I) and Stage II calcite vein (F8-4-stage II) at 8050.05 m depth in well F8-4 **(a1)**–**(a4)**. Stage III calcite vein (F8-4-stage III) and Stage IV calcite vein (F8-4-stage IV), fracture-filled, at 8049.50 m depth in well F8-4 **(b1)**–**(b4)**.

Yun, 2021a). However, these geophysical methods lack the temporal resolution required for precise chronological constraints, limiting their utility to broad stage approximations rather than absolute timing.

In this study, cathodoluminescence imaging coupled with in situ U-Pb geochronology of calcite veins within the Shunbei No. 4 fault system reveals two distinct Middle Caledonian calcite vein formation events in Well F4-5 (473 ± 12 Ma and 443 ± 17 Ma; Fig. 11(a)). These findings align with and refine prior geochronological studies, which identified multiple reactivation episodes spanning the Middle–Late Caledonian (472.69–456.68 Ma, 472.69–423.56 Ma, 449 ± 15 Ma, 449.41–415.36 Ma, 455.35–415.36 Ma, 433.48–423.56 Ma, and 433 ± 17 Ma), Late Caledonian–Early Hercynian (415 ± 8.57 Ma, 415.83–403.09 Ma, and 358.57–342.64 Ma), Middle–Late Hercynian (307.9 ± 82.1 Ma, 308.58–278.59 Ma, and 300.85–290.38 Ma), and Indosinian (248.59–215.01 Ma; Li et al., 2023; Peng et al., 2024; Song et al., 2022). By integrating our U-Pb constraints with existing seismic datasets, we propose a four-phase activation history for the Shunbei No. 4 fault: (1) Middle–Late Caledonian, (2) Late Caledonian–Early Hercynian, (3) Middle–Late Hercynian, and (4) Indosinian–Yanshanian (Fig. 11(a)). Seismic interpretations alone yield divergent classifications, with prior studies proposing either three phases (Middle Caledonian, Late Caledonian–Early Hercynian, and Middle–Late Hercynian; Liu and Deng, 2022; Liu et al., 2023) or four phases (including an Indosinian–Himalayan phase; Yun, 2021a). Our chronology

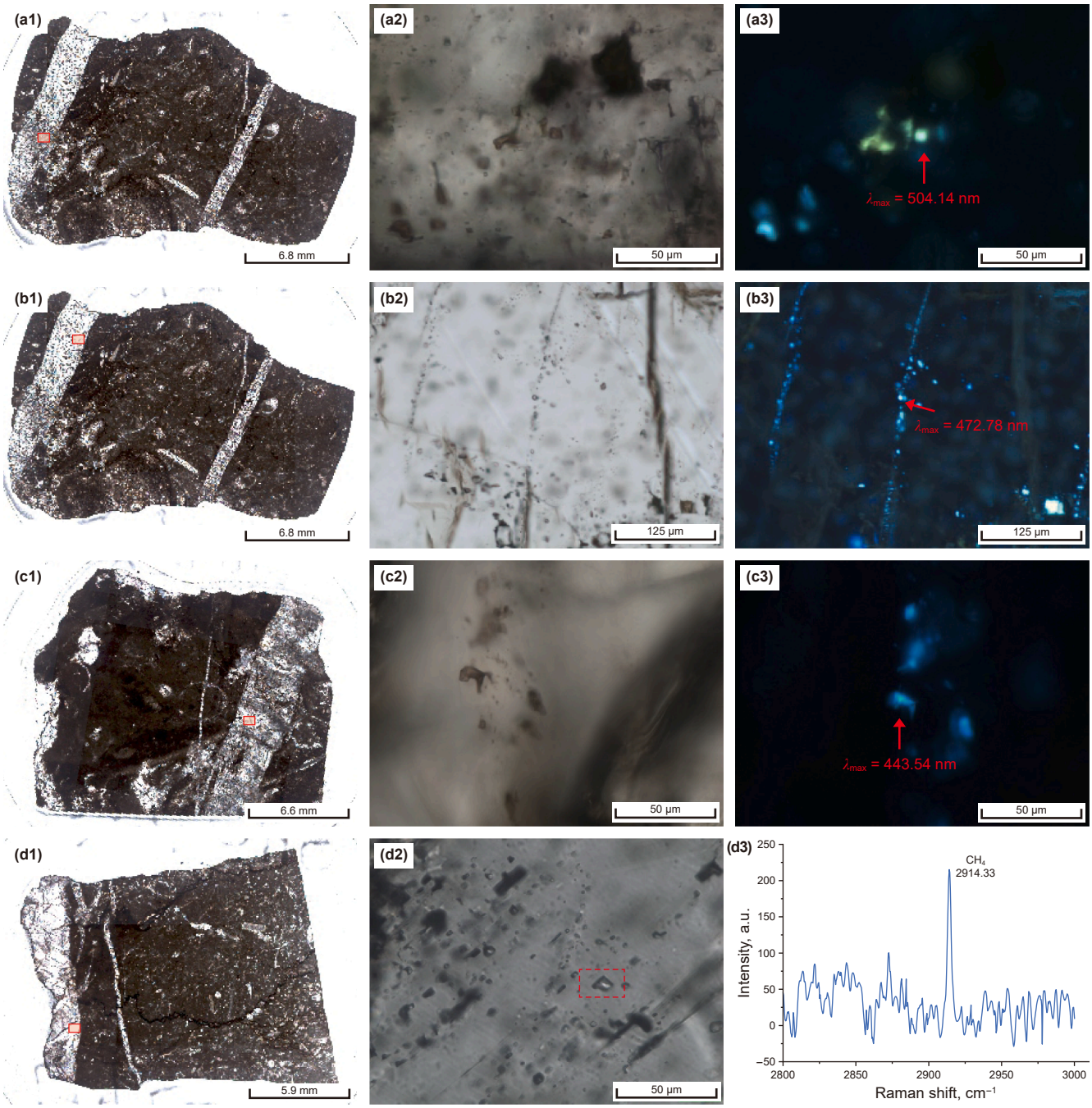

Fig. 6. **(a1)**, **(a2)**, **(b1)**, **(b2)**, **(c1)**, **(c2)**, **(d1)** and **(d2)** are representative photomicrographs under plane-polarized light. **(a3)**, **(b3)** and **(c3)** are corresponding images under ultraviolet light. λ_{max}—Wavelength of maximum intensity in the fluorescence spectrum. **(a1)**, **(b1)**, **(c1)**, **(d1)** Fracture-filling calcite vein from well F4-5 at a depth of 7727.28 m. **(a2)**–**(a3)** Primary yellow-green oil inclusion assemblages within the calcite vein. **(b2)**–**(b3)** Secondary pale blue oil inclusion assemblages within the calcite vein. **(c2)**–**(c3)** Secondary dark blue oil inclusion assemblages within the calcite vein. **(d2)**–**(d3)** Secondary methane inclusion assemblages within the calcite vein.

resolves these discrepancies by calibrating seismic reflectors with U-Pb ages, demonstrating that the Indosinian–Yanshanian phase corresponds to localized reactivation rather than basin-wide deformation. This integration significantly enhances temporal resolution compared to purely seismic-derived models.

For the Shunbei No. 8 strike-slip fault, previous geophysical analyses suggested a four-stage activity history (Middle Caledonian, Late Caledonian–Early Hercynian, Middle–Late Hercynian, and Indosinian–Yanshanian; Yun, 2021a), though precise timing remained unresolved. Our systematic cathodoluminescence and U-Pb analysis of calcite veins in Well F8-4 provides critical chronological constraints. In Well F8-4, four calcite generations record episodic fault reactivation: Middle Caledonian (453.5 ± 2.5 Ma), Late Caledonian–Early Hercynian (413 ± 29 Ma), Middle–Late Hercynian (294 ± 29 Ma), and Indosinian–Yanshanian (196 ± 57 Ma; Fig. 11(b)). The U-Pb age of the F8-4-stage IV calcite vein (196 ± 57 Ma) should be interpreted with caution due to its elevated common Pb content and significant analytical uncertainty. While this age broadly aligns with regional Indosinian–Yanshanian reactivation phases (Yun, 2021a; Liu et al., 2023), its low

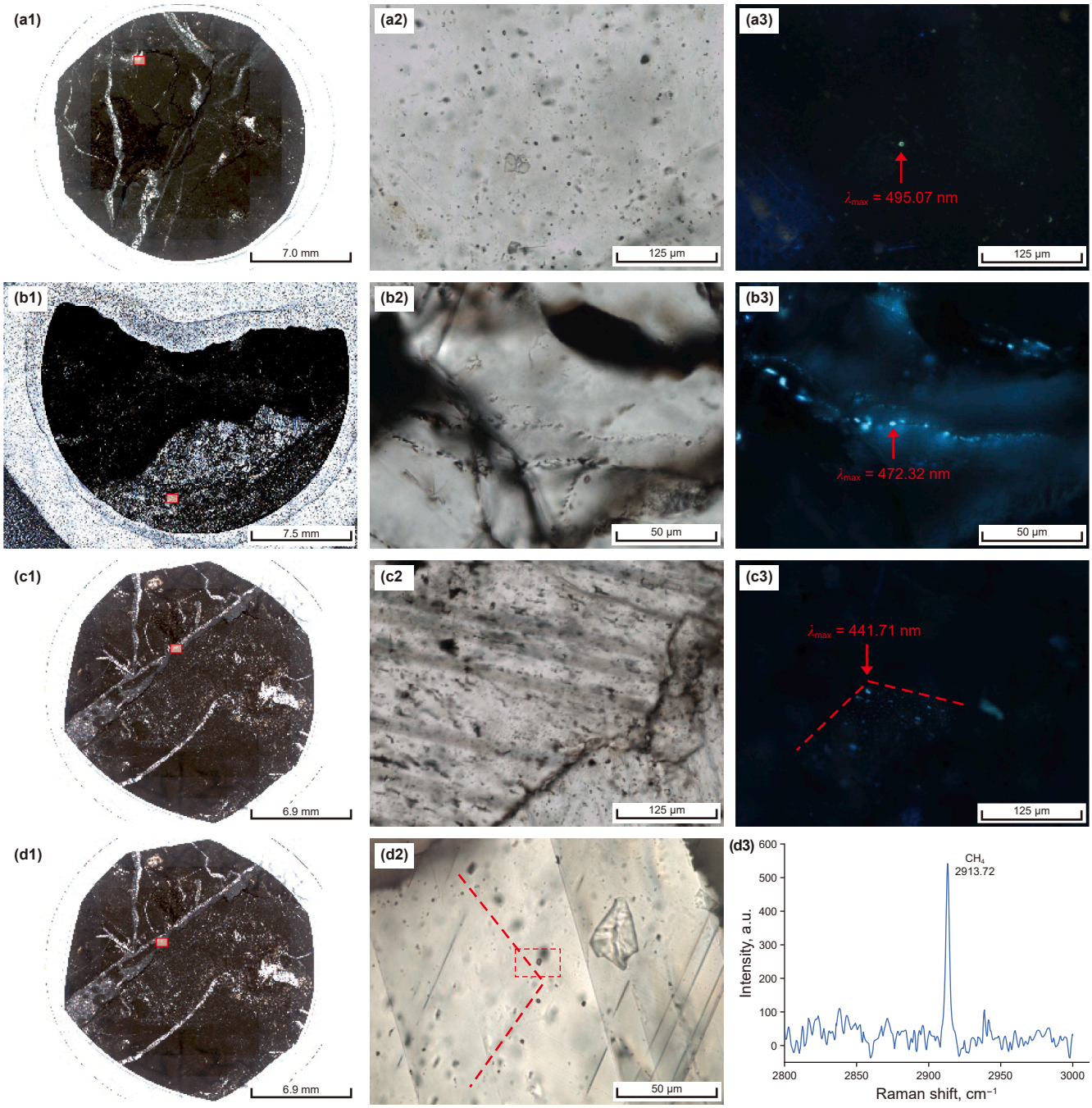

Fig. 7. **(a1)**–**(a3)** Primary yellow-green inclusion assemblages within the calcite vein from well F8-4 at 8050.05 m, under plane light and ultraviolet light. **(b1)**–**(b3)** Secondary pale blue inclusion assemblages within the calcite vein from well F8-4 at 8050.50 m, under plane light and ultraviolet light. **(c1)**–**(c3)** Primary dark blue inclusion assemblages within the calcite vein from well F8-4 at 8049.50 m, under plane light and ultraviolet light. **(d1)**–**(d3)** Primary methane inclusion assemblages within the calcite vein from well F8-4 at 8049.50 m.

precision precludes definitive chronological conclusions and is presented here as a provisional constraint.

Synthesizing our U-Pb geochronological results with prior geophysical interpretations (Yun, 2021a), we propose a four-stage activity history for the Shunbei No. 8 fault: Middle–Late Caledonian oblique compression (453.5 ± 2.5 Ma), Late Caledonian–Early Hercynian transtension (413 ± 29 Ma), Mid-Late Hercynian reactivation (294 ± 29 Ma), and Indosinian–Yanshanian structural overprinting (196 ± 57 Ma).

5.2. Determining the accumulation period of the ordovician reservoir within the shunbei no.4 and no.8 fault zones

Primary oil inclusions, which form synchronously with their host minerals during vein growth (Goldstein and Reynolds, 1994), serve as direct records of hydrocarbon charging events. By integrating these inclusions with U-Pb dating of their host calcite veins (Cong et al., 2022), we establish absolute chronologies for petroleum migration, resolving both the timing and duration of

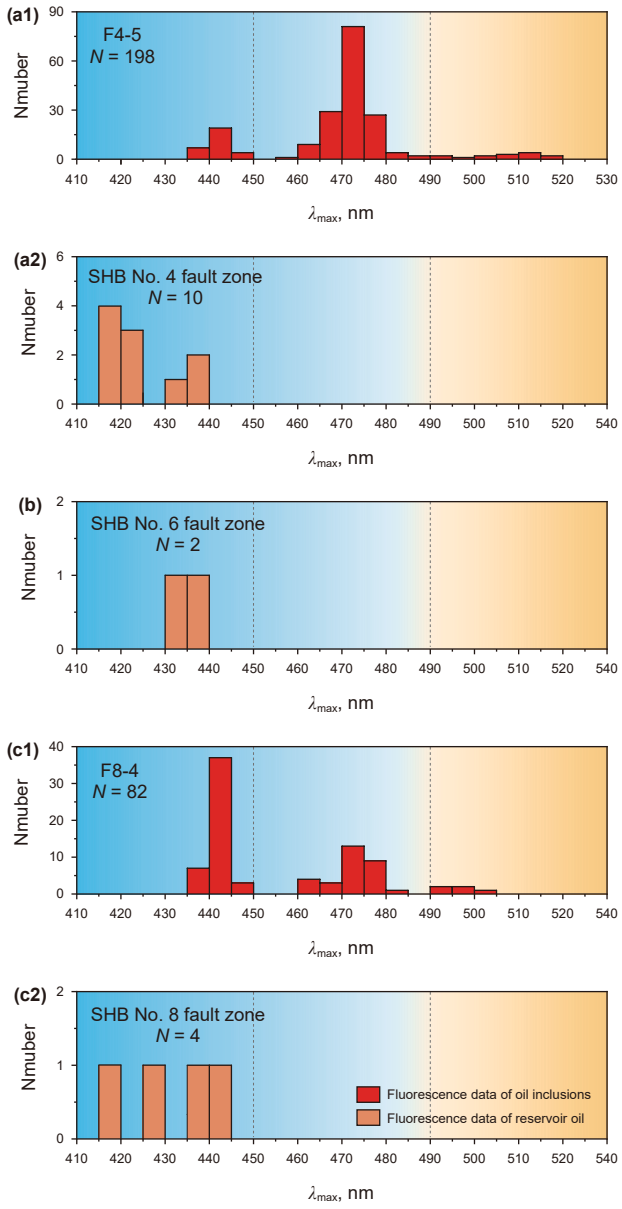

Fig. 8. Histograms of oil-inclusion and reservoir oil fluorescence spectra from fourteen wells located along the SHB No. 4 (wells F4-1, F4-2, F4-3, F4-4, F4-5, F4-6, F4-7, F4-8, F4-9 and F4-11), SHB No. 6 (wells F6-1 and F6-2) and SHB No. 8 (wells F8-1, F8-2, F8-3 and F8-4) fault zones.

hydrocarbon accumulation. In this study, fracture-filling calcite veins (F4-5-stage II and F8-4-stage I, III, IV) associated with distinct fault reactivation episodes were found to host primary hydrocarbon inclusions of varying thermal maturities. Secondary oil inclusions identified in F4-5-stage II and F8-4-stage II veins were analyzed using an integrated approach combining host mineral formation ages, aqueous inclusion homogenization temperatures (Th), and regional burial-thermal history models (Figs. 9 and 10).

For the Shunbei No. 4 fault zone (Well F4-5), four hydrocarbon charging phases were reconstructed. Secondary oil inclusions with yellow-green fluorescence (λ_{max} = 520–490 nm) and pale blue fluorescence (λ_{max} = 490–455 nm) correspond to Late Caledonian (443 ± 17 Ma) and Early–Middle Hercynian (415–295 Ma) charging events, respectively (Fig. 9). Dark blue fluorescent inclusions (λ_{max} = 450–435 nm) date to the Late Hercynian–Indosinian (282–205 Ma), while methane-dominated charging during the Yanshan–Himalayan (196–11 Ma) marks the final reservoir-filling phase (Fig. 9). This multi-stage accumulation history reflects progressive thermal maturation and fault-controlled migration pathways activated during successive tectonic episodes.

In the Shunbei No. 8 fault zone (Well F8-4), primary and secondary inclusions similarly delineate a polyphase charging sequence. Primary yellow-green inclusions (λ_{max} = 510–490 nm) in F8-4-stage I calcite date to the Middle Caledonian (453.5 ± 2.5 Ma), while secondary pale blue inclusions (λ_{max} = 485–460 nm) in F8-4-stage II veins record Middle–Late Caledonian activity (450–418 Ma; Fig. 10). Later stages include dark blue primary inclusions (λ_{max} = 450–435 nm) formed during the Middle–Late Hercynian (294 ± 29 Ma) and methane-dominated charging linked to Late Hercynian–Yanshan tectonism (196 ± 57 Ma; Fig. 10). These results demonstrate that hydrocarbon accumulation in the Ordovician reservoirs was episodic, tightly coupled to strike-slip fault reactivation and basin-scale thermal evolution.

The integration of fluorescence spectroscopy, microthermometry, and U-Pb chronometry resolves previously ambiguous timing relationships, establishing a robust temporal framework for hydrocarbon migration and entrapment. This approach not only constrains the absolute timing of charging events but also correlates them with specific fault activation phases, offering predictive insights for ultra-deep reservoir exploration in structurally complex basins.

5.3. Geochemical characteristics of oil and gas in the shunbei strike-slip faults and their main charge events

Petroleum, a complex mixture of hydrocarbon compounds (Wilhelms and Larter, 2004), exhibits geochemical parameters that serve as reliable proxies for assessing thermal maturity and identifying mixing processes. Methylated aromatic hydrocarbons, with their stable molecular structures, provide isomerization ratios (e.g., MPI-1 and MDR) effective for evaluating high-to over-mature oils. In the Shunbei No. 4, No. 6, and No. 8 fault zones, MPI-1 values indicate oils within high-mature to over-mature stages (Fig. 3(a)). The relationship between MDR and MPI-1 indicates that crude oils from selected wells (not all) in the Shunbei No. 4, 6, and 8 strike-slip fault systems have been influenced by hydrothermal fluids (Fig. 3(a)). Contrary to initial interpretations, the thermal maturity of these hydrothermal-affected oils is actually lower than values derived from geochemical parameters, leading to an overestimation of maturity (Xu et al., 2022). Diamondoids, thermally stable biomarkers enriched during advanced maturation (Chen et al., 1996; Dahl et al., 1999), further constrain maturity through methyladamantane (MAI) and methyldiamantane indices (MDI). MAI and MDI values (63.44%–73.53% and 43.77%–57.88%, respectively; Fig. 3(b)) correspond to equivalent vitrinite reflectance (R_o) values of 1.2%–1.6%, excluding two outliers in the SHB No. 4 fault. Heptane (H) and isoheptane (I) values, calibrated to Thompson's (1983) maturity framework, corroborate R_o >1.2% (Fig. 3(c)).

Pyrolysis experiments define three sequential oil-cracking stages: (1) Decomposition of NSO compounds (nitrogen-, sulfur-, and oxygen-containing organics), (2) Cracking of C_{15}^{+} hydrocarbons to C_6–C_{14} hydrocarbons and residual bitumen, and (3) Cracking of C_6–C_{14} hydrocarbons to C_1–C_5 gases (Dieckmann et al., 2000; Tian et al., 2009). Oils from the Shunbei No. 4 (excluding Well F4-2) and No. 6 fault zones exhibit methyldiamantane concentrations below 200 ppm (Fig. 3(d)), significantly lower than those in the Shunnan (SN) field. This indicates incomplete gas-phase cracking, consistent with light oil preservation during

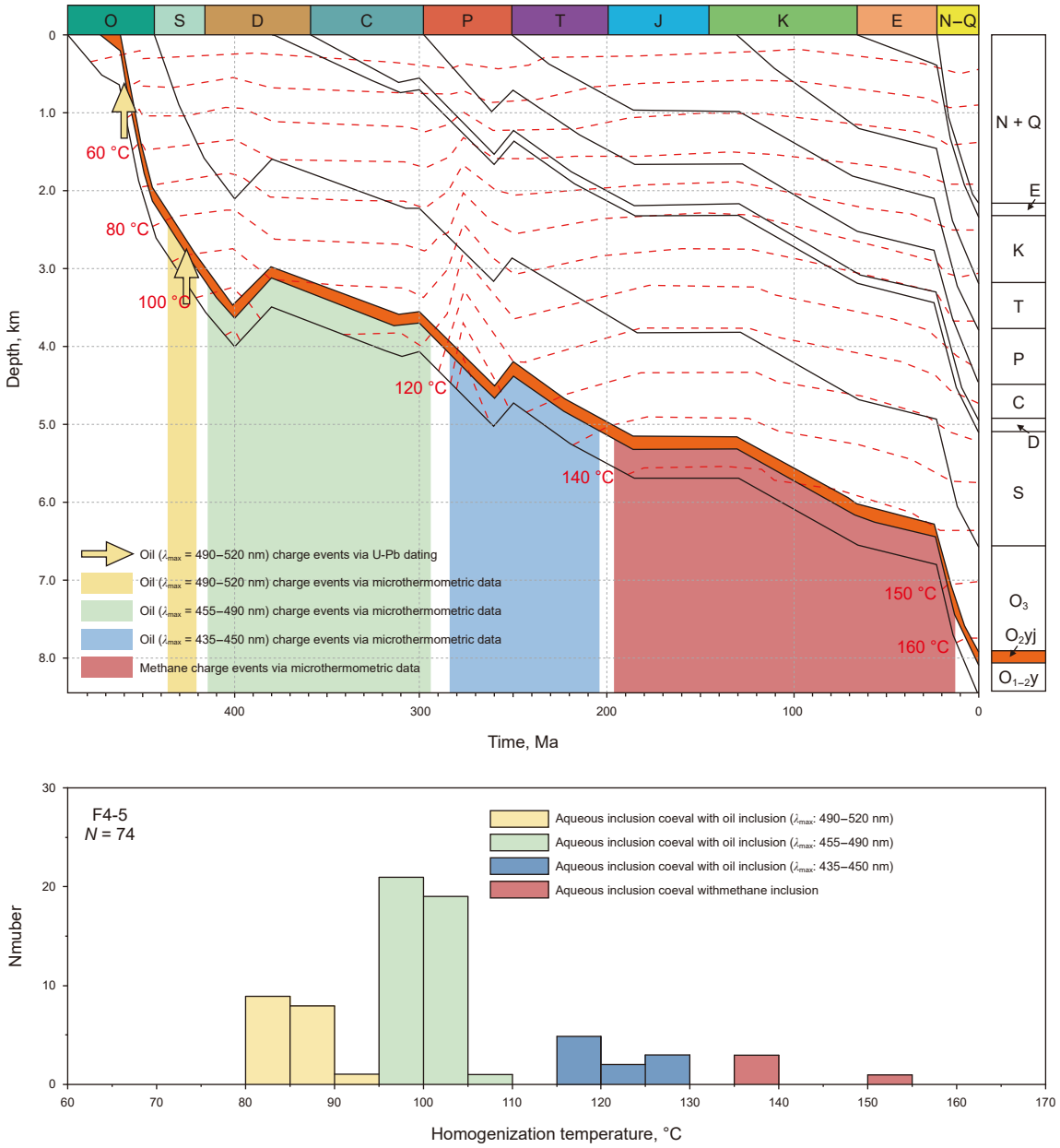

Fig. 9. Histogram of homogenization temperatures (Th) of hydrocarbon inclusions within well along the SHB No. 4 (well F4-5) fault zones. The thermal and burial history of well F4-5 suggests that the fluorescent yellow-green oil inclusions, with a λ_{max} ranging from 520 nm to 490 nm, were generated approximately between 435 and 420 Ma. The fluorescent pale blue oil inclusions, with a λ_{max} ranging from 455 to 490 nm, were generated approximately between 415 and 295 Ma. The fluorescent dark blue oil inclusions, with a λ_{max} ranging from 435 to 445 nm, were generated around 282 to 205 Ma. The methane inclusions were generated approximately between 196 and 11 Ma. Stratigraphic Formations: N-Q—Neogene–Quaternary; E—Paleogene; K—Cretaceous; J—Jurassic; T—Triassic; P—Permian; C—Carboniferous; D—Devonian; S—Silurian; O—Ordovician.

early maturation. In contrast, oils from the Shunbei No. 8 fault and Well F4-2 display elevated methyldiamantane levels relative to other Shunbei samples, though still lower than Shunnan oils, suggesting partial gas-phase cracking superimposed on light oil generation. The $\delta^{13}C_1$ (−49.48‰ to −44.21‰) and $\delta^{13}C_2$ (−40.31‰ to −36.17‰) values indicate that natural gas in the Shunbei area of the Tarim Basin predominantly resides within the normal genetic field, with no carbon isotope reversal ($\delta^{13}C_1 < \delta^{13}C_2$), reflecting characteristics of low-maturity oil-type gas (Wang et al., 2024; Zhang et al., 2017, 2021). Natural gas compositions, analyzed via $\ln(C_2/C_3)$ versus $\delta^{13}C_2$–$\delta^{13}C_3$ cross-plots (Prinzhofer and Huc, 1995), predominantly reflect kerogen-derived cracking gas (Fig. 3(f)). However, minor contributions from secondary oil cracking cannot be excluded.

Quantitative fluorescence spectroscopy reveals reservoir oils in the Shunbei fault zones exhibit fluorescence wavelengths <445 nm (Fig. 8), corresponding to R_o >1.26% (Ping et al., 2020). This high maturity aligns with geochemical indices, confirming advanced thermal evolution. Hydrocarbon charging histories for the No. 4 and No. 8 fault zones identify four distinct phases. The third phase, marked by oil inclusions with fluorescence wavelengths of 450–435 nm, correlates with present-day reservoir oils (λ_{max} = 445–410 nm). The absence of inclusions <435 nm likely reflects oil cracking during geological history, as cracked oils exhibit diminished fluorescence intensity.

In the Shunbei No. 4 fault zone, Cambrian reservoirs experienced peak thermal maturation (~160 °C) during the third hydrocarbon charging episode (282–205 Ma; corresponding to the

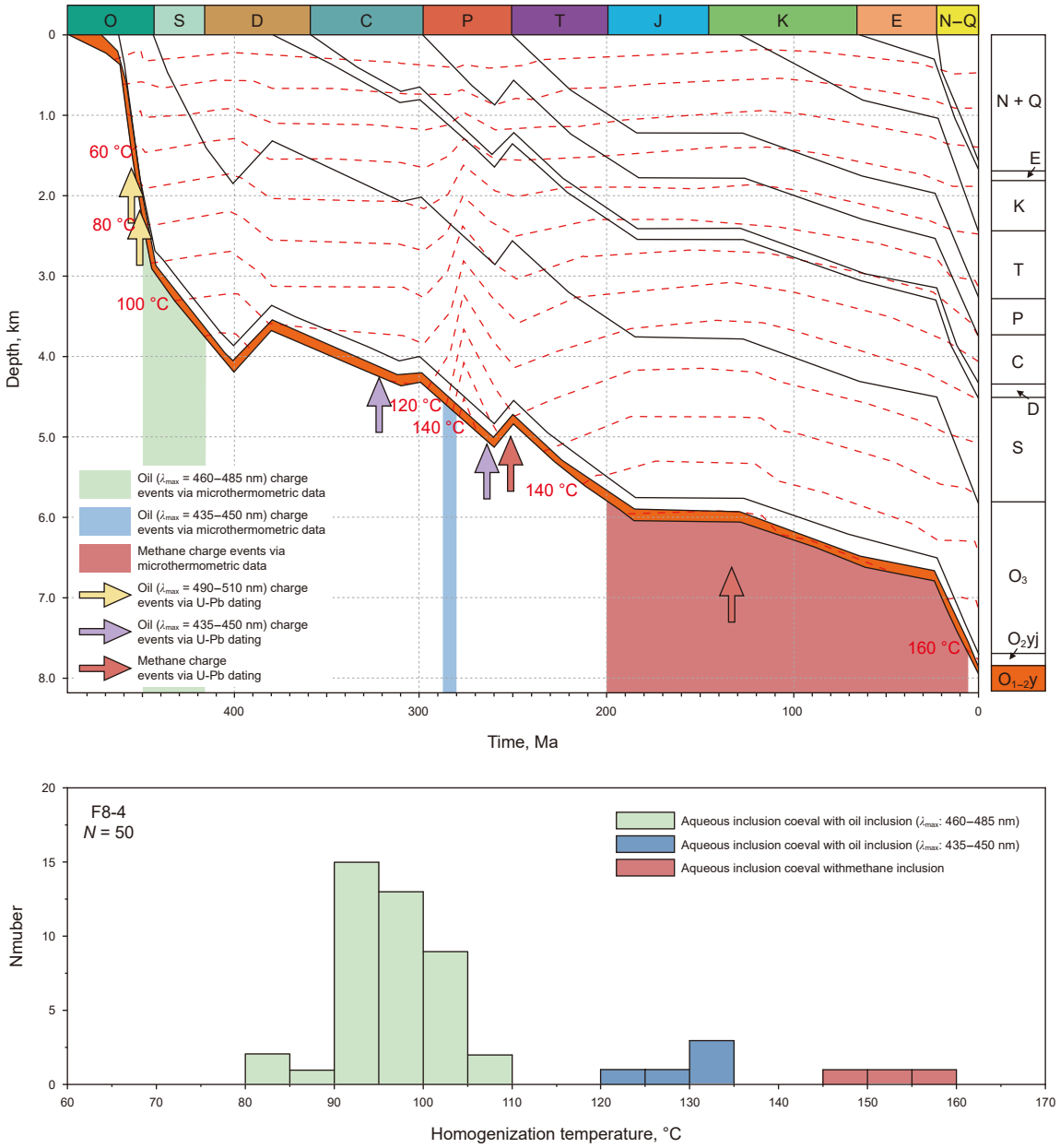

Fig. 10. Histogram of homogenization temperatures (Th) of hydrocarbon inclusions within well along the SHB No. 8 (well F8-4) fault zones. Well F8-4's thermal and burial history shows that the fluorescent yellow-green oil inclusions, with a λ_{max} ranging from 510 to 490 nm, were generated at 453.5 ± 2.5 Ma. The fluorescent pale blue oil inclusions, with a λ_{max} ranging from 485 to 460 nm, were generated approximately between 450 and 418 Ma. In contrast, the fluorescent dark blue oil inclusions, with a λ_{max} ranging from 450 to 435 nm, were generated approximately between 294 ± 29 Ma. Meanwhile, the methane inclusions were generated at 196 ± 57 Ma. Stratigraphic Formations: N-Q—Neogene–Quaternary; E—Paleogene; K—Cretaceous; J—Jurassic; T—Triassic; P—Permian; C—Carboniferous; D—Devonian; S—Silurian; O—Ordovician.

principal oil charging event in Ordovician reservoirs). This thermal regime initiated primary oil cracking processes, generating light hydrocarbons that subsequently migrated into overlying Ordovician reservoir units. The No. 8 fault zone exhibits contrasting thermal evolution: While its Ordovician reservoirs received direct light oil charging during the Middle Hercynian orogeny (294 ± 29 Ma; principal oil charging event), the underlying Cambrian reservoirs maintained subcritical temperatures (<160 °C) that effectively inhibited thermal cracking of hydrocarbons.

Late Hercynian to Indosinian tectonic activity facilitated secondary migration of minor cracked oil fractions, which co-transported with methane into Ordovician reservoirs through fracture networks. The terminal hydrocarbon charging phases occurred at 196–11 Ma (No. 4 fault zone) and 196 ± 57 Ma (No. 8 fault zone), corresponding to natural gas charging events that preferentially targeted Ordovician reservoir intervals. This multi-stage accumulation pattern demonstrates systematic vertical hydrocarbon migration from Cambrian source/cracking zones to Ordovician reservoir traps. These results highlight fault reactivation chronology as a primary control mechanism governing both hydrocarbon migration pathways and thermal maturation processes in ultra-deep (>6,000 m) carbonate reservoirs.

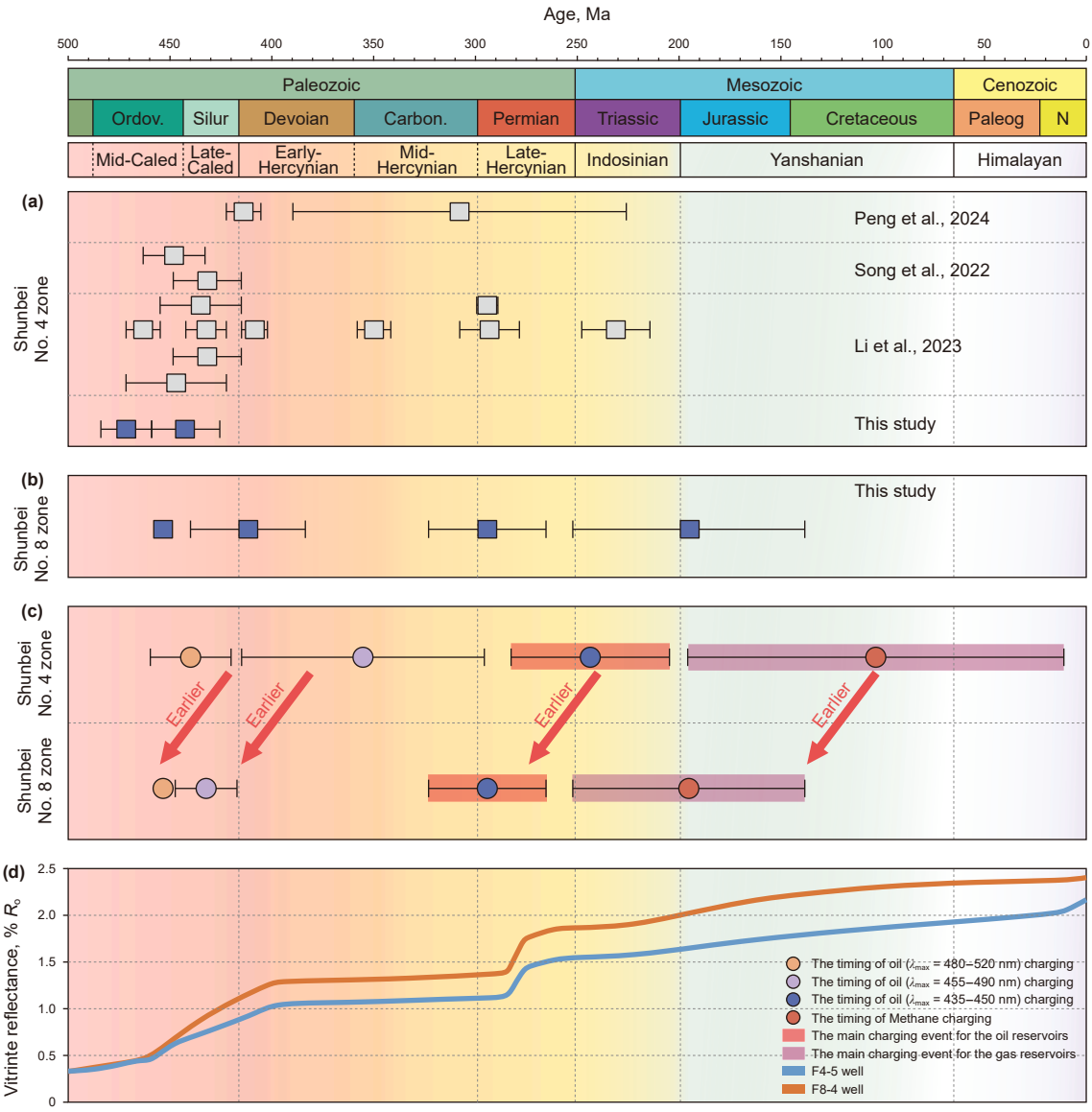

Fig. 11. **(a)**–**(b)** Temporal analysis of strike-slip fault activity in the SHB No. 4 and No. 8 fault zones, inferred from calcite U-Pb dating based on prior studies (Li et al., 2023; Peng et al., 2024; Song et al., 2022) and this research. **(c)** Chronological summary of oil and gas charging in the SHB No. 4 and No.8 fault zones (wells F4-5 and F8-4), determined using calcite U-Pb dating and fluid inclusion thermometry in this study. **(d)** Hydrocarbon generation history of the SHB No. 4 and No. 8 fault zones (wells F4-5 and F8-4).

5.4. Differential hydrocarbon charging pattern in the shunbei strike-slip fault systems

Hydrocarbon migration in the Tarim Basin's fault-controlled reservoirs is predominantly vertical, with the Cambrian Yuertusi Formation serving as the primary source rock (Liu Z. et al., 2024). This study integrates geochemical data, hydrocarbon charging events, and regional tectonic evolution to establish a differential accumulation model for the Shunbei No. 4 and No. 8 strike-slip fault systems (Fig. 12).

Middle Caledonian III phase: During this stage, NNW-oriented compression reactivated pre-existing faults in the Shuntuoguole area (Qiu et al., 2019; Deng et al., 2020; Yun, 2021a). In the Shunbei No. 8 fault, mature oil from the Yuertusi Formation migrated vertically into Cambrian–Ordovician reservoirs, forming early accumulations. These are recorded by primary yellow-green fluorescent oil inclusions (λ_{max}: 505–490 nm) sporadically distributed in calcite cements (Fig. 12(a)).

Late Caledonian phase (Fig. 12(b)): Oblique extension reactivated both faults, enabling hydrocarbon migration under tensile stress (Liu and Deng, 2022). In the Shunbei No. 4 fault, first-stage oil from the Yuertusi Formation charged Cambrian–Ordovician reservoirs, captured as primary inclusions with λ_{max} = 520–490 nm. Concurrently, the No. 8 fault experienced second-stage oil migration, preserved as pale blue fluorescent inclusions (λ_{max}: 485–460 nm).

Early–Middle Hercynian phase (Fig. 12(c)): Regional uplift sustained fault activity (Qi, 2016). The No. 4 fault channeled second-stage oil (λ_{max}: 490–455 nm) into Ordovician reservoirs via steep pathways, represented by secondary inclusions in late-stage calcite fractures. In contrast, the No. 8 fault accumulated third-stage oil (λ_{max}: 450–435 nm), partially preserved as primary inclusions along mineral growth zones. Intense tectonic uplift

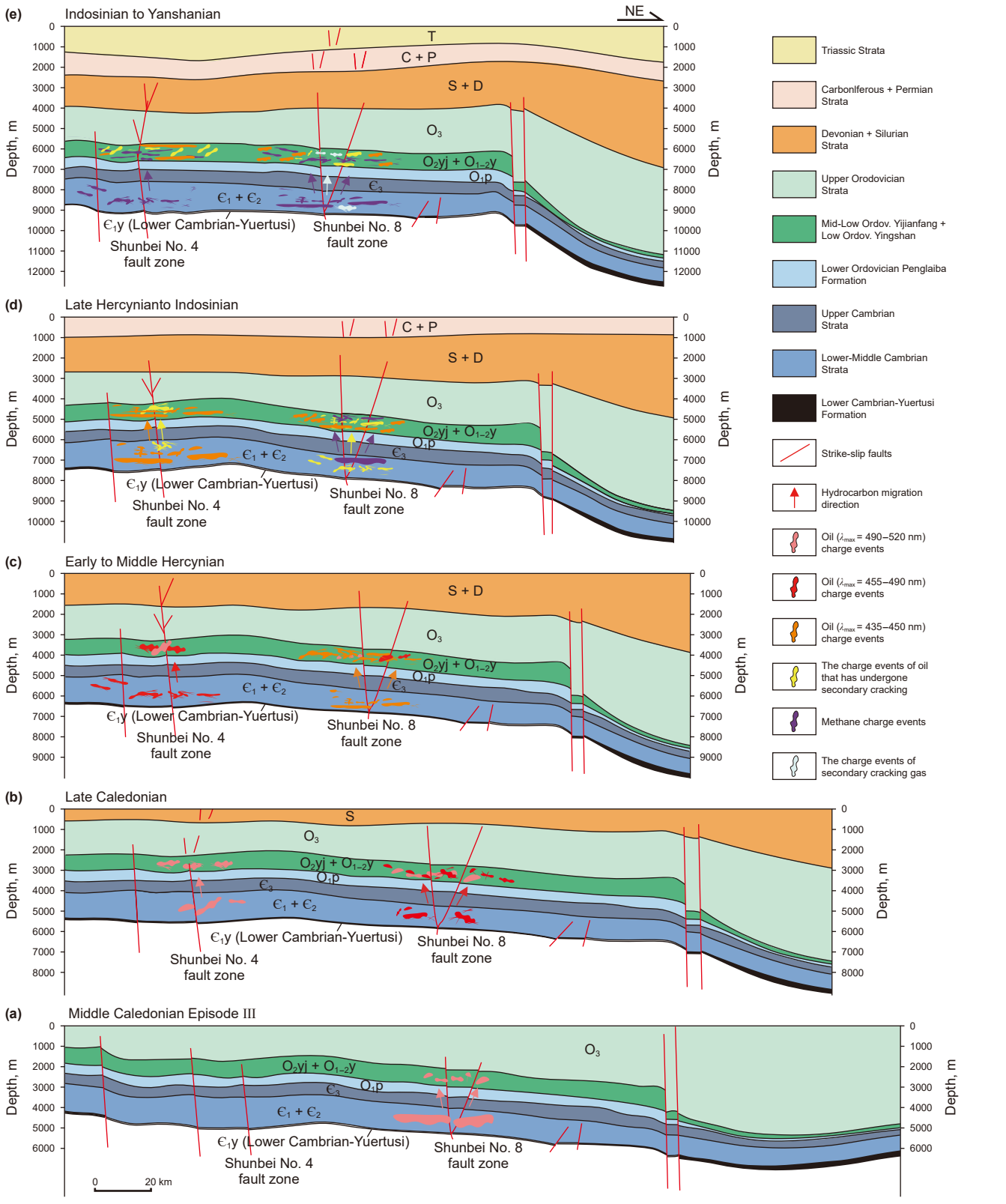

Fig. 12. Schematic diagram of hydrocarbon accumulation model in the eastern Shunbei area (Shunbei No. 4 and No. 8 strike-slip faults; section location indicated in Fig. 1(b), modified from Qi (2016); Chen et al. (2023).

during this phase likely disrupted earlier reservoirs in both systems (Wang B. et al., 2020).

Late Hercynian–Indosinian phase (Fig. 12(d)): In the No. 4 fault zone, Cambrian reservoirs approached critical thermal conditions (~160 °C), during which light oil (λ_{max}: 450–435 nm) was transported into these reservoirs. This temperature regime initiated the onset of early-stage oil cracking, resulting in a dual-phase hydrocarbon charge to overlying Ordovician reservoirs: (1) primary light oil directly migrated from Cambrian strata, and (2) minor early-cracked light oil derivatives. Concurrently, the No. 8 fault system channeled natural gas sourced from Yuertusi Formation source rocks into Ordovician strata, as evidenced by dominant methane fluid inclusions. Notably, localized Cambrian reservoirs in the No. 8 fault zone briefly exceeded 160 °C, enabling partial oil-to-light oil conversion, with subsequent upward migration of cracked products (Peng et al., 2024).

Indosinian–Yanshanian phase: Thermal intensification elevated the temperatures of Cambrian reservoirs in the No. 8 fault zone to approximately 170 °C, significantly accelerating oil-cracking processes. Meanwhile, reactivated faults in the No. 4 zone primarily facilitated gas migration. Within the Ordovician reservoirs of the No. 8 fault zone, trace amounts of oil-cracked gas became intermixed with kerogen-cracked gas, although the latter retained volumetric dominance (Fig. 12(e)).

Two principal factors account for this differential hydrocarbon charging history: First, source rock maturity beneath the Shunbei No. 8 fault system consistently exceeded that of the No. 4 system throughout geological history. As vertical migration dominates hydrocarbon transport in the Tarim Basin , hydrocarbon maturity directly reflects source rock evolution. Basin-wide recognition of the Yuertusi Formation as the primary source rock (Liu Z. et al., 2024) prompted comparative modeling of its hydrocarbon generation history beneath both fault zones. Results demonstrate systematically higher thermal maturation beneath the No. 8 system, enabling earlier generation of equivalent-maturity hydrocarbons compared to the No. 4 system.

Second, fault activity intensity in the Shunbei East Area (encompassing No. 4, 6, and 8 fault zones) exhibits a west-to-east increasing gradient (Yun, 2021a; Liu et al., 2023). Seismic-based analyses confirm that the No. 8 fault zone displays greater displacement magnitudes, weaker stratigraphic deformation, and enhanced vertical connectivity relative to adjacent systems (Liu et al., 2023). These structural characteristics promote more efficient vertical hydrocarbon migration in the No. 8 zone, explaining its earlier charging chronology compared to the No. 4 system.

The differential hydrocarbon enrichment between the Shunbei No. 1 and No. 5 strike-slip faults is primarily controlled by contrasting late-stage fault activity intensities (Cong et al., 2024a, 2024b). The principal hydrocarbon charging event in the Ordovician reservoirs of the Shunbei No. 1 fault occurred during the Himalayan period, whereas that in the Shunbei No. 5 fault took place in the Late Caledonian. This discrepancy arises because the relatively weak late-stage activity of the Shunbei No. 5 fault facilitated hydrocarbon retention within deep to ultra-deep Cambrian reservoirs, while the stronger late-stage activity of the Shunbei No. 1 fault promoted hydrocarbon migration into shallower Ordovician reservoirs.

For the Shunbei No. 4 and No. 8 strike-slip faults, the systematic differences in hydrocarbon enrichment are governed by variations in fault activity intensity and the thermal maturity of underlying Yuertusi Formation source rocks. The Shunbei No. 8 fault exhibits greater displacement magnitude, enhanced vertical connectivity (Yun, 2021a; Liu et al., 2023), and higher thermal maturity of subjacent Yuertusi source rocks during equivalent geological periods compared to the No. 4 fault. These two primary factors collectively result in systematically earlier timing of multi-phase oil and gas charging events in the Ordovician reservoirs of the Shunbei No. 8 fault relative to those in the No. 4 fault. Consequently, the principal hydrocarbon charging events in the Ordovician reservoirs of the No. 8 fault also occurred earlier than those in the No. 4 fault system.

This integrated analysis reveals the coupled controls of intracratonic strike-slip fault dynamics and source rock maturation on hydrocarbon accumulation patterns. The proposed model emphasizes the critical interplay between fault reactivation histories, thermal evolution, and vertical migration efficiency in governing hydrocarbon distribution, providing predictive criteria for exploration in analogous strike-slip systems.

6. Conclusions

This study integrates crude oil and natural gas geochemistry, calcite U-Pb dating, and fluid inclusion analysis to constrain the timing of multi-phase activity within strike-slip fault systems. This multi-proxy approach resolves the complete reactivation history of these faults, provides absolute age constraints for hydrocarbon charging events, and identifies the principal timing of reservoir charge. By reconstructing differential hydrocarbon accumulation processes across distinct strike-slip systems, we advance the mechanistic understanding of ultra-deep, fault-controlled hydrocarbon enrichment, offering insights applicable to future exploration strategies in analogous fault-dominated reservoirs. Key findings include:

(1) Integrated geochemical and isotopic analyses reveal thermally mature hydrocarbons (R_o = 1.2%–1.6%; λ_{max} < 445 nm) in the Shunbei Nos. 4/6/8 fault systems, with diamondoid indices confirming oil-cracking processes. Gas compositions ($\delta^{13}C_1$ vs. $\delta^{13}C_2$; $\ln(C_2/C_3)$ vs. $\delta^{13}C_2$–$\delta^{13}C_3$) indicate low-maturity oil-type gas within the normal genetic field ($\delta^{13}C_1 < \delta^{13}C_2$), dominated by kerogen-cracked methane with minor oil-cracked contributions

(2) High-resolution chronostratigraphic constraints from integrated U-Pb dating, cathodoluminescence textures, and seismic sequence analysis delineate four discrete activation episodes for the Shunbei No. 4 and No. 8 faults: Middle–Late Caledonian (stage I), Late Caledonian–Early Hercynian (stage II), Middle–Late Hercynian (stage III), and Indosinian–Yanshanian (stage IV). This multi-proxy approach resolves previous dating discrepancies, delivering absolute temporal constraints for ultra-deep strike-slip systems.

(3) The Shunbei No. 8 fault exhibits systematic precedence in hydrocarbon charging across four tectonic phases relative to the No. 4 system: (i) Middle Caledonian oil migration (453.5 ± 2.5 Ma) vs. Late Caledonian phase (443 ± 17 Ma), (ii) Middle–Late Caledonian charging (450–418 Ma) vs. Early–Middle Hercynian activity (415–295 Ma), (iii) principal oil accumulation at 294 ± 29 Ma (Middle–Late Hercynian) vs. 282–205 Ma (Late Hercynian-Indosinian), and (iv) major gas charging at 196 ± 57 Ma (Late Hercynian-Yanshan) vs. 196–11 Ma (Yanshan-Himalayan). This multi-phase chronological advantage stems from the enhanced activity of the No.8 strike-slip fault, the high thermal maturity of source rocks, and the improved vertical permeability within the fault system, demonstrating that the charging chronology of intracratonic strike-slip reservoirs is fundamentally governed by the coupled evolution of fault activity, source rock thermal maturation, and fault conduit architecture.

CRediT authorship contribution statement

Zhuo Liu: Writing – review & editing, Writing – original draft, Investigation, Data curation, Conceptualization. **Jin-Qiang Tian:** Writing – review & editing, Supervision, Resources, Funding acquisition, Formal analysis, Conceptualization. **Fang Hao:** Resources, Funding acquisition, Conceptualization. **Yong-Li Liu:** Supervision, Resources. **Meng-Ting Hang:** Visualization, Validation, Methodology. **Fei-Fei Yuan:** Writing – review & editing, Methodology. **Fu-Yun Cong:** Methodology, Conceptualization.

Declaration of competing interest

The authors declare that they have no known competing financial interests or personal relationships that could have appeared to influence the work reported in this paper.

Acknowledgments

This study was funded by National Natural Science Foundation of China – Enterprise Joint Fund for Innovation and Development (U24B6001), National Natural Science Foundation of China (grant 42488101, grant 42172160 and grant 42202142), National Science and Technology Major Project (2025ZD1400502, 2025ZD1400507) and Taishan Scholars Project (No. ZX20250154).

Appendix A. Supplementary data

Supplementary data to this article can be found online at https://doi.org/10.1016/j.petsci.2025.09.022.

References

Aydin, A., Berryman, J.G., 2010. Analysis of the growth of strike-slip faults using effective medium theory. J. Struct. Geol. 32 (11), 1629–1642. https://doi.org/10.1016/j.jsg.2009.11.007.

Bian, J., Hou, D., Cui, Y., Zhu, X., 2023. Geochemical characteristics and origin of the ultra-deep hydrocarbons from the Shunbei oilfield in the Tarim Basin, China: Insight from molecular biomarkers and carbon isotope geochemistry. Mar. Petrol. Geol. 158, 106542. https://doi.org/10.1016/j.marpetgeo.2023.106542.

Cai, X., Li, Y., 2008. Ordovician lithofacies and stratigraphic lacunae in the southern part of the Central Tarim, Xinjiang. J. Stratigr. 32 (4), 353–362.

Cao, Z., Lu, Q., Gu, Y., Wu, X., You, D., Zhu, X., 2020. Characteristics of Ordovician reservoirs in Shunbei 1 and 5 fault zones, Tarim Basin. Oil & Gas Geol. 41 (5), 975–984. https://doi.org/10.11743/ogg20200508 (in Chinese).

Cao, Z., Yun, L., Qi, L., Li, H., Han, J., Geng, F., Lin, B., Chen, J., Hunag, C., Mao, Q., 2024. A major discovery of hydrocarbon-bearing layers over 1,000-meter thick in well Shunbei 84X, Shunbei area, Tarim Basin and its implications. Oil Gas Geol. 45 (2), 341–356 (in Chinese).

Celestino, M.A.L., Miranda, T.S., Mariano, G., Alencar, M.L., Buckman, J., Roberts, N.M.W., Barbosa, J.A., Neumann, V.H.M.L., Souza, J.A.B., Roemers-Oliveira, E., 2021. Structural control and geochronology of Cretaceous carbonate breccia pipes, Crato Formation, Araripe Basin, NE Brazil. Mar. Petrol. Geol. 132, 105190. https://doi.org/10.1016/j.marpetgeo.2021.105190.

Chen, H., 2023. Advances on relationship between strike-slip structures and hydrocarbon accumulations in Large superimposed Craton basins, China. Earth Sci. 48 (6), 2039–2066.. https://doi.org/10.3799/dqkx.2023.094 (in Chinese).

Chen, J., Fu, J., Sheng, G., Liu, D., Zhang, J., 1996. Diamondoid hydrocarbon ratios: novel maturity indices for highly mature crude oil. Org. Geochem. 25, 179–190. https://doi.org/10.1016/S0146-6380(96)00125-8.

Chen, J., Guo, X., Tao, Z., Cao, Z., Wang, B., Zhang, X., Xu, H., Zhao, J., 2022. U-Pb dating of oil charge in superimposed basins: A case study from the Tarim Basin, NW China. Geol. Soc. Am. Bull. 134 (11–12), 3176–3188. https://doi.org/10.1130/B36324.1.

Chen, Q., Ma, Z., Li, M., Xi, B., Zheng, L., Zhuang, X., Yuan, K., Ma, X., Xu, J., 2023. Mechanisms of liquid hydrocarbon evolution and preservation in ultradeep Ordovician reservoirs, northern Tarim Basin: Insights from laboratory simulation experiments. Earth Sci. Front. 30 (6), 329–340. https://doi.org/10.13745/j.esf.sf.2023.2.13 (in Chinese).

Cong, F.Y., Tian, J.Q., Hao, F., Andrew, R.C., Kylander-Clark, Pan, W.J., Zhang, B.S., 2022. Calcite U-Pb ages constrain petroleum migration pathways in tectonic complex basins. Geology 50 (6), 644–649. https://doi.org/10.1130/G49750.1.

Cong, F., Tian, J., Hao, F., Licht, A., Liu, Y., Cao, Z., Eiler, J.M., 2021. A thermal pulse induced by a Permian mantle plume in the Tarim Basin, Northwest China: Constraints from clumped isotope thermometry and in situ calcite U-Pb dating. J. Geophys. Res. Solid Earth 126, 1–27. https://doi.org/10.1029/2020JB020636.

Cong, F., Tian, J., Hao, F., Wang, Q., Liu, J., Cao, Z., 2024a. Differential petroleum charging controlled by movements of two strike-slip faults in the Shunbei area, Tarim Basin, Northwestern China. AAPG Bull. 108, 877–906. https://doi.org/10.1306/12152319179.

Cong, F., Tian, J., Hao, F., Wang, Q., Kylander-Clark, A.R.C., Cao, Z., 2024b. In-situ calcite U-Pb ages and absolute timing of oil charge events: A case study of ultra-deep carbonate reservoirs in the Shunbei oilfield, Tarim Basin, Northwest China. J. Asian Earth Sci. 259, 105904. https://doi.org/10.1016/j.jseaes.2023.105904.

Craddock, J.P., Nuriel, P., Kylander-Clark, A.R.C., Hacker, B.R., Luczaj, J., Weinberger, R., 2021. Long-term (7 Ma) strain fluctuations within the Dead Sea transform system from high-resolution U-Pb dating of a calcite vein. Geol. Soc. Am. Bull. 134 (5–6), 1231–1246. https://doi.org/10.1130/B36000.1.

Dahl, J.E., Moldowan, J.M., Peters, K.E., Claypool, G.E., Rooney, M.A., Michael, G.E., Mello, M.R., Kohnen, M.L., 1999. Diamondoid hydrocarbons as indicators of natural oil cracking. Nature 399, 54–57.

Dai, J., Xoa, X., Li, Z., Coleman, D.D., Dias, R.F., Gao, L., Li, J., Deev, A., Li, J., Dessort, D., Duclerc, D., Li, L., Liu, J., Schloemer, S., Zhang, W., Ni, Y., Hu, G., Wang, X., Tang, Y., 2012. Inter-laboratory calibration of natural gas round robins for δ^2H and δ^{13}C using off-line and on-line techniques. Chem. Geol. 310–311, 49–55. https://doi.org/10.1016/j.chemgeo.2012.03.008.

Deng, S., Li, H., Zhang, Z., Wu, X., Zhang, J., 2018. Characteristics of differential activities in major strike-slip fault zones and their control on hydrocarbon enrichment in Shunbei area and its surroundings, Tarim Basin. Oil Gas Geol. 39 (5), 878–888. https://doi.org/10.11743/ogg20180503 (in Chinese).

Deng, S., Li, H., Zhang, Z., Zhang, J., Yang, X., 2019. Structural characterization of intracratonic strike-slip faults in the central Tarim Basin. AAPG Bull. 103 (1), 109–137. https://doi.org/10.1306/06071817354.

Deng, S., Liu, Y., Liu, J., Han, J., Wang, B., Zhao, R., 2020. Structural styles and evolution models of intracratonic strike-slip faults and the implications for reservoir exploration and appraisal: A case study of the Shunbei area, Tarim Basin. Geotect. Metallogenia 45 (6), 1111–1126.. https://doi.org/10.16539/j.ddgzyckx.2020.05.015 (in Chinese).

Deng, S., Qiu, H., Liu, D., Han, J., Ru, Z., Peng, W., Bian, Q., Huang, C., 2024. Advances in research on the genetic mechanisms of intracratonic strike-slip fault system and their control on hydrocarbon accumulation: A case study of the northern Tarim Basin. Oil Gas Geol. 45 (5), 1211–1225. https://doi.org/10.11743/ogg20240502 (in Chinese).

Deng, S., Zhao, R., Kong, Q., Li, Y., Li, B., 2022. Two distinct strike-slip fault networks in the Shunbei area and its surroundings, Tarim Basin: Hydrocarbon accumulation, distribution, and controlling factors. AAPG (Am. Assoc. Pet. Geol.) Bull. 106 (1), 77–102. https://doi.org/10.1306/07202119113.

Dieckmann, V., Schenk, H.J., Horsfield, B., 2000. Assessing the overlap of primary and secondary reactions by closed- versus open-system pyrolysis of marine kerogens. J. Anal. Appl. Pyrolysis 56, 33–46.

Dong, S., Han, J., Zhao, J., You, D., 2025. LA-ICP-MS U-Pb geochronology of calcites reveals multiphase tectonic activities and associated fluid flow in Western Shunbei area, NW China. Sci. China Earth Sci. 68 (4), 1180–1188. https://doi.org/10.1007/s11430-024-1515-1.

He, B.Z., Jiao, C.L., Xu, Z.Q., Cai, Z.H., Zhang, J.X., Liu, S.L., Li, H.B., Chen, W.W., Yu, Z.Y., 2016. The paleotectonic and paleogeography reconstructions of the Tarim Basin and its adjacent areas (NW China) during the late early and Middle Paleozoic. Gondwana Res. 30, 191–206. https://doi.org/10.1016/j.gr.2015.09.011.

He, K., Zhang, S.C., Wang, X.M., Mi, J.K., Zhang, W.J., Guo, J.H., Zhang, W.L., 2021. Pyrolysis of 1-methylnaphthalene involving water: Effects of Fe-bearing minerals on the generation, C and H isotope fractionation of methane from H_2O-hydrocarbon reaction. Org. Geochem. 152, 104151. https://doi.org/10.1016/j.orggeochem.2020.104151.

Goldstein, R.H., Reynolds, T.J., 1994. Systematics of fluid inclusions in diagenetic minerals. In: SEPM Short Course, vol. 31, pp. 1–199.

He, S., Deng, S., Liu, Y., Qiu, H., Zhu, X., Li, C., 2023. New structural style of spatial Architecture and derived structure of intracratonic strike-slip faults: A case study of Shunbei No. 12 fault, Tarim Basin. Earth Sci. 48 (6), 2136–2150.. https://doi.org/10.3799/dqkx.2022.495 (in Chinese).

Holdsworth, R.E., McCaffrey, K.J.W., Dempsey, E., Roberts, N.M.W., Hardman, K., Morton, A., Feely, M., Hunt, J., Conway, A., Robertson, A., 2019. Natural fracture propping and earthquake-induced oil migration in fractured basement reservoirs. Geology 47, 700–704. https://doi.org/10.1130/G46280.1.

Jia, C., Wei, G., 2002. Structural characteristics and petroliferous features of Tarim Basin. Chin. Sci. Bull. 47, 1–11. https://doi.org/10.1007/BF02902812.

Jia, C., Ma, D., Yuan, J., Wei, G., Yang, M., Yan, L., Tian, F., Jiang, L., 2022. Structural characteristics, formation & evolution and genetic mechanisms of strike–slip faults in the Tarim Basin. Nat. Gas. Ind. B 9, 51–62. https://doi.org/10.1016/j.ngib.2021.08.017.

Li, C., Wang, X., Li, B., He, D., 2013. Paleozoic fault systems of the Tazhong uplift, Tarim Basin, China. Mar. Petrol. Geol. 39, 48–58. https://doi.org/10.1016/j.marpetgeo.2012.09.010.

Li, D., Liang, D., Jia, C., Wang, G., Wu, Q., He, D., 1996. Hydrocarbon accumulations in the Tarim Basin, China. AAPG Bull. 80 (10), 1587–1603. https://doi.org/10.1306/64eda0be-1724-11d7-8645000102c1865d.

Li, H., Gao, J., Cao, Z., Zhu, X., Guo, X., Zeng, S., 2023. Spatial-temporal distribution of fluid activities and its significance for hydrocarbon accumulation in the

strike-slipfault zones, shuntuoguole low-uplift, Tarim Basin. Earth Sci. Front. 30 (6), 316–328. https://doi.org/10.13745/j.esf.sf.2023.2.36 (in Chinese).
Li, M., Wang, T., Chen, J., He, F., Yun, L., Akbar, S., Zhang, W., 2010. Paleo-heat flow evolution of the Tabei uplift in Tarim Basin, Northwest China. J. Asian Earth Sci. 37, 52–66. https://doi.org/10.1016/j.jseaes.2009.07.007.
Liu, B., Zhao, Y., Zhang, Y., Zhou, F., Xie, Z., Yao, C., Yin, S., Ding, L., Zhao, L., Sun, C., 2025. Structural analysis and reservoir-controlling significance of No. 19 strike-slip fault in the eastern Aman transition zone, Tarim Basin. Earth Sci. Front. 32 (4), 301-316. https://doi.org/10.13745/j.esf.sf.2025.2.1 (in Chinese).
Liu, J., Cai, Z., Teng, C., Zhang, H., Chen, C., 2023. Coupling relationship between formation of calcite veins and hydrocarbon charging in Middle-Lower Ordovician reservoirs in strike-slip fault zones within craton in Shunbei area, Tarim Basin. Oil Gas Geol. 44 (1), 125–137. https://doi.org/10.11743/ogg20230110 (in Chinese).
Liu, X., Tian, J.Q., Hao, F., Zhang, Z., Yang, X.Z., Chen, Y.Q., Zhang, K., Wang, X.X., Cong, F.Y., 2024. The generation mechanism of deep natural gas in Tabei uplift, Tarim Basin, Northwest China: Insights from instantaneous and accumulative effects. Pet. Sci. 21, 3804–3814. https://doi.org/10.1016/j.petsci.2024.08.002.
Liu, Y., Deng, S., 2022. Structural analysis of intraplate strike slip faults with small to medium displacement: A case study of the Shunbei 4 fault, Tarim Basin. J. China Inst. Min. Univ. 51 (1), 124–136. https://doi.org/10.13247/j.cnki.jcumt.001324 (in Chinese).
Liu, Y., Deng, S., Zhang, J., Qiu, H., Han, J., He, S., 2023. Characteristics and formation mechanism of the strike-slip fault networks in the Shunbei area and the surroundings, Tarim Basin. Earth Sci. Front. 30 (6), 95–109. https://doi.org/10.13745/j.esf.sf.2023.2.31 (in Chinese).
Liu, Z., Tian, J., Hao, F., Yang, X., Chen, Y., Zhang, K., Wang, X., Quan, L., Cong, F., 2024. The hydrocarbon generation process of the deeply buried Cambrian Yuertusi Formation in the Tabei Uplift, Tarim Basin, northwestern China: Constraints from calcite veins hosting oil inclusions in the source rock. Geol. Soc. Am. Bull. 136 (9/10), 3810–3824. https://doi.org/10.1130/B37295.1.
Lu, Z., Chen, H., Qing, H., Chi, G., You, D., Yin, H., Zhang, S., 2017. Petrography, fluid inclusion and isotope studies in Ordovician carbonate reservoirs in the Shunnan area, Tarim Basin, NW China: Implications for the nature and timing of silicification. Sediment. Geol. 359, 29–43. https://doi.org/10.1016/j.sedgeo.2017.08.002.
Lueck, R.L., Fischer, M.P., Williams, N.J., Drost, K., Dodd, J.P., Chew, D.M., 2021. A two-stage, fault-controlled paleofluid system at the southern termination of the Gypsum Valley salt wall, Paradox Basin. Colorado, USA. Basin Res. 34 (3), 1020–1054. https://doi.org/10.1111/bre.12649.
Ma, A., Qi, L., 2023. Geochemical characteristics and phase behavior of the Ordovician ultra-deep reservoir fluid, No.4 fault, northern Shuntuoguole, Tarim Basin. Earth Sci. Front. 30 (6), 247–262. https://doi.org/10.13745/j.esf.sf.2023.2.21 (in Chinese).
Ma, Y., Cai, X., Yun, L., Li, Z., Li, H., Deng, S., Zhao, P., 2022. Practice and theoretical and technical progress in exploration and development of Shunbei ultra-deep carbonate oil and gas field, Tarim Basin, NW China. Petrol. Explor. Dev. 49 (1), 1–20. https://doi.org/10.1016/j.marpetgeo.2021.105063.
Ma, Y., He, Z., Zhao, P., Zhu, H., Han, J., You, D., Zhang, J., 2019. A new progress in formation mechanism of deep and ultra-deep carbonate reservoir. Acta Pet. Sin. 40 (12), 1415–1425 (in Chinese).
Mann, P., 2007. Global catalogue, classification and tectonic origins of restraining and releasing bends on active and ancient strike-Slip fault systems. Geol. Soc. 290 (1), 13–142. https://doi.org/10.1144/sp290.2.
Norris, A., Danyushevsky, L., 2018. Towards estimating the complete uncertainty budget of quantified results measured by LA-ICP-MS. In: Goldschmidt Conference, Boston. https://goldschmidtabstracts.info/2018/1894.pdf.
Nuriel, P., Wotzlaw, J.F., Ovtcharova, M., Vaks, A., Kylander-Clark, A.R.C., 2021. The use of ASH-15 flowstone as a matrix-matched reference material for laser-ablation U-Pb geochronology of calcite. Geochronology 3 (1), 35–47. https://doi.org/10.5194/gchron-3-35-2021.
Peng, W., Deng, S., Zhang, J., Huang, C., Qiu, H., Li, Y., Liu, Y., Liu, D., 2024. Genetic mechanism and main controlling factors of deep marine condensate reservoirs: A case study of the shunbei No.4 fault zone in Tarim Basin, NW China. Nat. Gas Geosci. 35 (5), 838–850. https://doi.org/10.11764/j.issn.1672-1926.2024.04.008 (in Chinese).
Ping, H., Chen, H., George, S.C., 2020. Quantitatively predicting the thermal maturity of oil trapped in fluid inclusions based on fluorescence and molecular geochemical data of oil inclusions in the dongying depression, Bohai Bay basin, China. AAPG (Am. Assoc. Pet. Geol.) Bull. 108, 1751–1791. https://doi.org/10.1306/09271919096.
Prinzhofer, A.A., Huc, A.Y., 1995. Genetic and post-genetic molecular and isotopic fractionations in natural gases. Chem. Geol. 126, 281–290. https://doi.org/10.1016/0009-2541(95)00123-9.
Qi, J., Chen, S., Luo, C., Huang, S., Neng, Y., 2024. Strike-slip fault system andits reservoir-controlling rulesin Awati-Manger-transitional area, Tarim Basin. Acta Geol. Sin. 98 (12), 3662–3682 (in Chinese).
Qi, L., 2016. Oil and gas breakthrough in ultra-deep Ordovician carbonate formations in shuntuoguole uplift, Tarim Basin. China Petrol. Explor. 21 (3), 38–51. https://doi.org/10.3969/j.issn.1672-7703.2016.03.004 (in Chinese).
Qi, L., 2020. Characteristics and inspiration of ultra-deep fault-karst reservoir in the Shunbei area of the Tarim Basin. China Petrol. Explor. 25 (1), 102–111. https://doi.org/10.3969/j.issn.1672-7703.2020.01.010 (in Chinese).
Qi, L., Yun, L., Cao, Z., Li, H., Huang, C., 2021. Geological reserves assessment and petroleum exploration targets in shunbei oil & gas field. Xinjing Pet. Geol. 42 (2), 2168–2188. https://doi.org/10.7657/XJPG20210201 (in Chinese).
Qiao, R., Li, M., Zhang, D., Xiao, H., 2024a. Distribution and origin of higher diamondoids in the ultra-deep Paleozoic condensates of the Shunbei oilfield in the Tarim Basin, NW China. Org. Geochem. 197 (2024), 104883. https://doi.org/10.1016/j.orggeochem.2024.104883.
Qiao, R., Li, M., Zhang, D., Xiao, H., 2024b. Geochemistry and accumulation of the ultra-deep Ordovician oils in the Shunbei oilfield, Tarim Basin: Coupling of reservoir secondary processes and filling events. Mar. Petrol. Geol. 167, 106959. https://doi.org/10.1016/j.marpetgeo.2020.104725.
Qiu, H., Deng, S., Cao, Z., Yin, T., Zhang, Z., 2019. The evolution of the complex anticlinal belt with crosscutting strike-slip faults in the central Tarim Basin, NW China. Tectonics 38, 2087–2113. https://doi.org/10.1029/2018TC005229.
Radke, M., 1988. Application of aromatic compounds as maturity indicators in source rocks and crude oils. Mar. Petrol. Geol. 5, 224–236. https://doi.org/10.1016/02648172(88)90003-7.
Radke, M., Welte, D.H., Willsch, H., 1986. Maturity parameters based on aromatic hydrocarbons: Influence of the organic matter type. Org. Geochem. 10 (1–3), 51–63. https://doi.org/10.1016/0146-6380(86)90008-2.
Roberts, N.M.W., Walker, R.J., 2016. U-Pb geochronology of calcite-mineralized faults: Absolute timing of rift-related fault events on the northeast Atlantic margin. Geology 44 (7), 531–534. https://doi.org/10.1130/G37868.1.
Rochelle-Bates, N., Roberts, N.M.W., Sharp, I., Freitag, U., Verwer, K., Halton, A., Fiordalisi, E., van Dongen, B.E., Swart, R., Ferreira, C.H., Dixon, R., Schröder, S., 2021. Geochronology of volcanically associated hydrocarbon charge in the pre-salt carbonates of the Namibe Basin, Angola. Geology 49 (3), 335–340. https://doi.org/10.1130/G48019.1.
Song, G., Li, H., Ye, N., Han, J., Xiao, C., Lu, Z., Li, Y., 2022. Types and features of diagenetic fluids in Shunbei No. 4 strike-slipfault zone in Shuntuoguole Low Uplift, Tarim Basin. Petrol. Geol. Exp. 44 (4), 603–612. https://doi.org/10.11781/sysydz202204603 (in Chinese).
Tang, D., Chen, H., Geng, F., Qi, R., Jiang, H., Guzailinuer, A., 2023. Characteristics of intraplate small-displacement strike-slip faults: A case study of Tarim, Sichuan and ordos basins. Earth Sci. 48 (6), 2067–2086. https://doi.org/10.3799/dqkx.2023.037 (in Chinese).
Teng, C., Cai, Z., Hao, F., Cao, Z., 2020. Structural geometry and evolution of an intracratonic strike-slip fault zone: A case study from the north SB5 fault zone in the Tarim Basin, China. J. Struct. Geol. 140, 104159. https://doi.org/10.1016/j.jsg.2020.104159.
Thompson, K.F.M., 1983. Classification and thermal history of petroleum based on light hydrocarbons. Geochem. Cosmochim. Acta 47, 303–316.
Tian, H., Xiao, X., Yang, L., Xiao, Z., Guo, L., Shen, J., Lu, Y., 2009. Pyrolysis of oil at high temperatures: Gas potentials, chemical and carbon isotopic signatures. Chin. Sci. Bull. 54, 1217–1224.
Vermeesch, P., 2018. IsoplotR: A free and open toolbox for geochronology. Geosci. Front. 9, 1479–1493. https://doi.org/10.1016/j.gsf.2018.04.001.
Walter, B.F., Gerdes, A., Kleinhanns, I.C., Dunkl, I., Eynatten, H., Kreissl, S., Markl, G., 2018. The connection between hydrothermal fluids, mineralization, tectonics and magmatism in a continental rift setting: Fluorite Sm-Nd and hematite and carbonates U-Pb geochronology from the Rhinegraben in SW Germany. Geochem. Cosmochim. Acta 240 (2018), 11–42. https://doi.org/10.1016/j.gca.2018.08.012.
Walters, C.C., Isaksen, G.H., Peters, K.E., 2003. Applications of light hydrocarbon molecular and isotopic compositions in oil and gas exploration. In: Hsu, C.S. (Ed.), Analytical advances for hydrocarbon research. Modern Analytical Chemistry. Springer, Boston, MA.
Wang, B., Zhao, Y., He, S., Guo, X., Cao, Z., Deng, S., Wu, X., Yang, Y., 2020. Hydrocarbon accumulation stages and their controlling factors in the northern Ordovician Shunbei 5 fault zone, Tarim Basin. Oil Gas Geol. 41 (5), 965–974. https://doi.org/10.11743/ogg20200507 (in Chinese).
Wang, J., Wang, X., Cao, Y., Hao, F., Pang, Y., Yun, L., Yang, H., Xie, M., 2024. Characteristics and origin of the ultradeep Ordovician faultkarst reservoirs: An example from the Shunbei-Yuejin area, Tarim Basin. AAPG (Am. Assoc. Pet. Geol.) Bull. 108 (7), 1231–1260. https://doi.org/10.1306/10052321152.
Wang, M., Chen, Y., Bain, W.M., Song, G., Liu, K., Zhou, Z., Steele-MacInnis, M., 2020. Direct evidence for fluid overpressure during hydrocarbon generation and expulsion from organic-rich shales. Geology 48, 374–378. https://doi.org/10.1130/G46650.1.
Wang, Q., Hao, F., Cao, Z., Tian, J., Cong, F., 2021. Geochemistry and origin of the ultra-deep Ordovician oils in the Shunbei field, Tarim Basin, China: Implications on alteration and mixing. Mar. Petrol. Geol. 123, 104725. https://doi.org/10.1016/j.marpetgeo.2020.104725.
Wang, Q., Yang, H., Li, Y., Lü, X., Zhang, Y., Zhang, Y., Sun, C., Ouyang, S., 2022a. Control of strike-slip fault on the large carbonate reservoir in Fuman Tarim Basin-a reservoir model. Earth Sci. Front. 29 (6), 239–251. https://doi.org/10.13745/j.esf.sf.2022.8.17 (in Chinese).
Wang, Z., Gao, Z., Fan, T., Zhang, H., Yuan, Y., Wei, D., Qi, L., Yu, L., Karubandika, G.M., 2022b. Architecture of strike-slip fault zones in the central Tarim Basin and implications for their control on petroleum systems. J. Petrol. Sci. Eng., 110432 https://doi.org/10.1016/j.petrol.2022.110432.
Wilhelms, A., Larter, S., 2004. In: Shaken but Not Always Stirred. Impact of Petroleum Charge Mixing on Reservoir Geochemisty. Geological Society Special Publication 237, 27–35.

Wu, G., Ma, B., Han, J., Guan, B., Chen, X., Yang, P., Xie, Z., 2021. Origin and growth mechanisms of strike-slip faults in the central Tarim cratonic Basin, NW China. Petrol. Explor. Dev. 48 (3), 595–607. https://doi.org/10.1016/S1876-3804(21)60048-4.

Wu, S., Yang, Y., Roberts, N.M.W., Yang, M., Wang, H., Lan, Z., Xie, B., Li, T., Xu, L., Huang, C., Xie, L., Yang, J., Wu, F., 2022. In situ calcite U-Pb geochronology by high-sensitivity single-collector LA-SF-ICP-MS. China Earth Sci. 65 (6), 1146–1160. https://doi.org/10.1007/s11430-021-9907-1.

Xu, H., Liu, Q., Jin, Z., Zhu, D., Meng, Q., Wu, X., Li, P., Zhu, B., 2024. Organic compounds in geological hydrothermal systems: A critical review of molecular transformation and distribution. Earth Sci. Rev. 252, 104757. https://doi.org/10.1016/j.earscirev.2024.104757.

Xu, H., Liu, Q., Zhu, D., Peng, W., Meng, Q., Wang, J., Shi, J., Jin, Z., 2022. Molecular evidence reveals the presence of hydrothermal effect on ultra-deep-preserved organic compounds. Chem. Geol. 608, 121045. https://doi.org/10.1016/j.chemgeo.2022.121045.

Yang, H., Li, Y., Ma, D., Wei, H., Li, H., Luo, C., Zhao, Y., Duan, Y., Huang, T., Zhao, T., 2022a. The mid-paleozoic extensional structures revealed in the eastern Tarim Basin and their geological significance. Chin. J. Geol. 57 (3), 633–652. https://doi.org/10.12017/dzkx.2022.037 (in Chinese).

Yang, P., Liu, K., Li, Z., Alexander, M.B.I., Liu, J., 2022b. Evolution of Ordovician YJ1X ultra-deep oil reservoir in the Yuecan oilfield, Tarim Basin, NW China. Petrol. Explor. Dev. 49 (2), 300–312. https://doi.org/10.1016/S1876-3804(22)60025-9.

Yang, P., Wu, G., Nuriel, P., Nguyen, A.D., Chen, Y., Yang, S., Feng, Y., Ren, Z., Zhao, J., 2021. In situ LA-ICPMS U–Pb dating and geochemical characterization of fault-zone calcite in the central Tarim Basin, Northwest China: Implications for fluid circulation and fault reactivation. Chem. Geol. 568. https://doi.org/10.1016/j.chemgeo.2021.120125.

Yao, Z., He, G., Li, C.F., Dong, C., 2018. Sill geometry and emplacement controlled by a major disconformity in the Tarim Basin, China. Earth Planet Sci. Lett. 501, 37–45. https://doi.org/10.1016/j.epsl.2018.08.026.

Yun, L., 2021a. Controlling effect of NE strike-slip fault system on reservoir development and hydrocarbon accumulation in the eastern Shunbei area and its geological significance, Tarim Basin. China Petrol. Explor. 26 (3), 41–52. https://doi.org/10.3969/j.issn.1672-7703.2021.03.004 (in Chinese).

Yun, L., 2021b. Hydrocarbon accumulation of ultra-deep Ordovician fault-karst reservoirs in shunbei area. Xinjing Pet. Geol. 42 (2), 136–142. https://doi.org/10.7657/XJPG20210202 (in Chinese).

Yun, L., Cao, Z., Geng, F., Wang, Y., Ding, Y., Liu, Y., 2025. Regularity of the Ordovician hydrocarbon system distribution in the Tabei nonforeland area of the Tarim Basin. Oil Gas Geol. 46 (1), 15–30. https://doi.org/10.11743/ogg20250102 (in Chinese).

Zhang, C.L., Zou, H.B., Li, H.K., Wang, H.Y., 2013. Tectonic framework and evolution of the Tarim Block in NW China. Gondwana Res. 23, 1306–1315. https://doi.org/10.1016/j.gr.2012.05.009.

Zhang, D., Li, M., Qiao, R., Xiao, H., 2024. Applicability and limitation of aromatic maturity parameters in high-maturity oil from ultradeep reservoirs. Energy Fuels 38, 18413–18430. https://doi.org/10.1021/acs.energyfuels.4c02159.

Zhang, S., He, K., Hu, G., Mi, J., Ma, Q., Liu, K., Tang, Y., 2017. Gases in the Paleozoic marine formations in the Sichuan Basin, SW China: Isotope fractionation of deep and high mature carbonate reservoir gases. Mar. Petrol. Geol. 1–15. https://doi.org/10.1016/j.marpetgeo.2017.02.010.

Zhang, S., He, K., Wang, X., Hu, G., Zhang, B., Mi, J., Su, J., 2021. The multi-path gas generation model and its potential contribution to petroleum accumulation in deep formations. Nat. Gas Geosci. 32 (10), 1421–1435. https://doi.org/10.11764/j.issn.1672-1926.2021.08.013 (in Chinese).

Zhang, S., Huang, H., Su, J., Liu, M., Wang, X., Hu, J., 2015. Geochemistry of Paleozoic marine petroleum from the Tarim Basin, NW China: Part 5. Effect of maturation, TSR and mixing on the occurrence and distribution of alkyldibenzothiophenes. Org. Geochem. 86, 8–18. https://doi.org/10.1016/j.orggeochem.2015.05.008.

Zhang, S., Huang, H., Xiao, Z., Liang, D., 2005. Geochemistry of Palaeozoic marine petroleum from the Tarim Basin, NW China. Part 2: Maturity assessment. Org. Geochem. 36, 1215–1225.

Zhang, S., Su, J., Wang, X., Zhu, G., Yang, H., Liu, K., Li, Z., 2011. Geochemistry of Palaeozoic marine petroleum from the Tarim Basin, NW China: Part 3. Thermal cracking of liquid hydrocarbons and gas washing as the major mechanisms for deep gas condensate accumulations. Org. Geochem. 42, 1394–1410. https://doi.org/10.1016/j.orggeochem.2011.08.013.

Zhang, Y., Cao, Z., Chen, H., Gu, R., Li, H., 2023a. Difference of hydrocarbon charging events and their contribution percentages to Ordovician reservoirs among strike-slip fault belts in Shunbei area, Tarim Basin. Earth Sci. 48 (6), 2168–2188. https://doi.org/10.3799/dqkx.2023.103 (in Chinese).

Zhang, Y., Chen, S., Liu, Q., Feng, G., Xie, Z., Liang, X., Li, T., Song, X., Kang, P., Peng, Z., 2023b. Development characteristics and evolution model of F_I19 fault in fuman Oilfield, Tarim Basin. Geoscience 37 (2), 10–20. https://doi.org/10.19657/j.geoscience.1000-8527.2022.058 (in Chinese).

Zhao, Z., Shi, W., 2019. LA-(MC-) ICP-MS U-Pb dating technique of calcite and its application in brittle structures. J. Earth Sci. Environ. 41 (5), 505–516 (in Chinese).

Zhu, G., Milkov, A.V., Zhang, Z., Sun, C., Zhou, X., Chen, F., Han, J., Zhu, Y., 2019. Formation and preservation of a giant petroleum accumulation in superdeep carbonate reservoirs in the southern Halahatang oil field area, Tarim Basin, China. AAPG Bull. 103 (7), 1703–1743. https://doi.org/10.1306/11211817132.